Analysis of Elastic Energy during the Cutting of Bone

A thesis

Submitted By

Robert Ginsberg

IN PARTIAL FULFILLMENT OF THE REQUIREMENTS
FOR THE DEGREE OF

MASTER OF SCIENCE

IN

MECHANICAL ENGINEERING

School of Engineering
Tufts University

August 2011
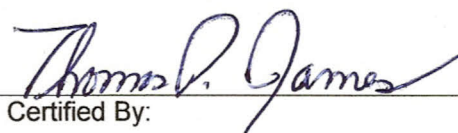
ADVISER: THOMAS JAMES PH.D.

Analysis of Elastic Energy during the

Cutting of Bone

May 2011

Signature of Author:
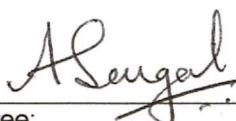
Robert Ginsberg

Certified By:

Thomas P. James, PhD
Assistant Professor
Department of Mechanical Engineering
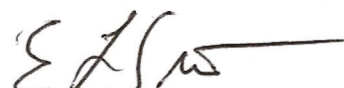School of Engineering
Tufts University

Committee:

Anil Saigal, PhD
Professor
Department of Mechanical Engineering
School of Engineering
Tufts University

Committee:

Eric Smith, MD
Chief of Arthroplasty, Tufts Medical Center
Assistant Professor
Department of Orthopaedic Surgery
School of Medicine
Tufts University

Abstract

A fixture was designed and manufactured that allowed for the measurement of energy absorbed during single tooth cutting of bovine bone. This fixture was utilized to evaluate the significance of the elastic compression of bone during cutting at depths of cut representative of sagittal or reciprocating bone sawing, used in orthopedic surgery. Experiments were completed recording position and forces during the cutting event in order to evaluate this elastic effect. By comparing the work of the force in the cutting direction, and the energy lost during the cutting event, calculated from kinetic energy, it was shown that elastic compression has no significant impact on the energy required to cut bone.

Acknowledgements

I would like to thank Professor Tom James for his support during my adventures of this thesis.

I would also like to thank my family for their support throughout the years, and my pre-wife, Ricki, for things too numerous to name.

Table of Contents

List of Figures

List of Tables

Introduction

In the current world of orthopedics, there are numerous injuries and conditions that necessitate surgery for correction of these ailments. Many of these operations also require the resection, removal, or cutting of sections of bone in order to remove damaged bone structures or create an acceptable location for mounting and attachment of a medical device [1]. The devices used for this bone removal process are power bone saws, and are of two main types as shown in Figure 1. The first type of saw is sagittal, a type of saw where the blade oscillates in a plane rapidly through a small angle, typically less than 5°, and the second type of saw is reciprocating, where the blade reciprocates linearly in a plane in order to remove material.

Figure 1: Power saw blade motion for a) reciprocating saw, b) sagittal saw. [2]

During these invasive procedures, it is important for the surgeons to utilize these saws as quickly as possible so that local increases in temperature from cutting and the overall operation time are minimized. It has been shown that temperatures of 50° C have significant negative effects on bone cells, including cell death, necrosis, and prevention of proper cell healing and regeneration [3]. A secondary factor that leads surgeons to quick saw utilization is the cost of occupying the operating room, which can be on the order of $75 per minute or higher [4]. This high cost of time in the operating room, which surgeons must justify to insurance companies, causes power saw operators to utilize them at high speeds with a large amount of force applied in order to cut through the bone quickly. This "all or nothing" mentality leads to large amounts of heat generation at the saw-bone interface, which has been studied by numerous researchers as to the effects of temperature increases [5,6,7]. However, these researchers have not studied the mechanisms which cause this heat generation nor the amount of energy introduced into the bone system by the process of cutting. This research seeks to evaluate the contribution of the elastic deformation of bone during cutting for the energy required to cut, and therefore, to the heat generation during cutting.

A typical power saw functions by applying a force on the saw toward the work piece and moving the saw against the work piece material, causing the saw teeth to cut into the work piece, as shown in Figure 2.
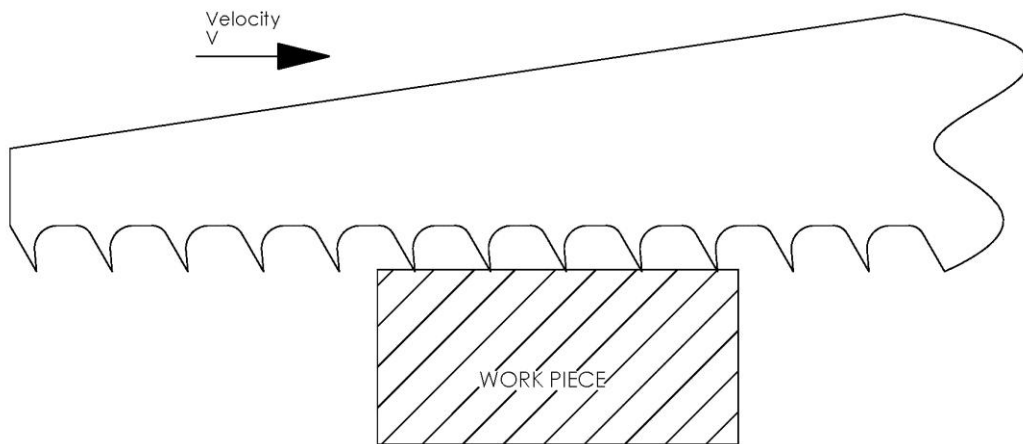
Figure 2: A saw blade cutting a work piece

As the blade moves parallel to the work piece, the pressure increases at the tooth/work interface, and eventually, this pressure becomes large enough that the work material shears against the saw tooth, physically removing material. Several geometry factors on saw blades have an impact on the forces and energy generated and used while cutting materials.
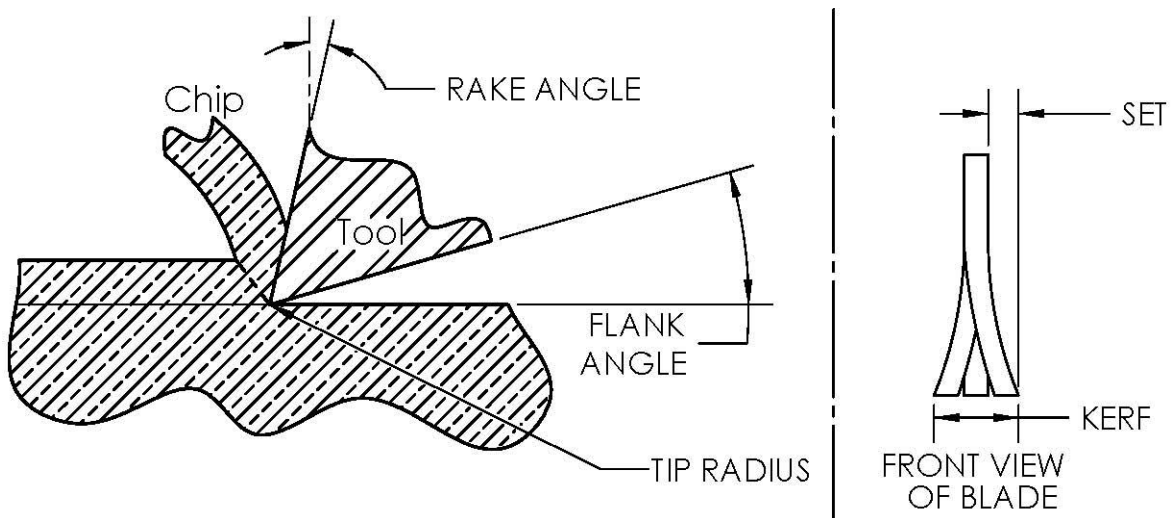
Figure 3: Geometry of a typical saw blade

The most commonly discussed variables are the tooth set, the bend distance of the tooth to the side of the blade, and the rake angle, the angle between the front face of

the tool and a line perpendicular to the direction of the cut, as shown in Figure 3. These two variables have an influence on the forces involved during cutting, and there is abundant research detailing these interactions in metal cutting, and some in bone cutting. However, the focus of this research is not on the geometry of the tooth, and will therefore, utilize a single style of saw tooth geometry throughout.

When examining the types of saws discussed for cutting bone, a common factor is a large number of teeth along the cutting surface, known as the tooth pitch, measured in mm between teeth (teeth per inch). A typical bone saw may have anywhere from 1.3 mm – 2.1 mm tooth spacing (12-20 teeth per inch TPI), a specification standard which helps users determine which saw to utilize for their particular cutting situation [8]. Previous research has been completed by Lannin and Kelly that measured bone cutting rates, which also resulted in the calculation of depth of cut per tooth on the particular saws used, with a tooth spacing of 1.4 mm (18 TPI). This depth of cut is on the order of 1 μm (.00004"), and, as shown in Figure 4, is of a smaller order of magnitude than the saw tooth tip radius [9,10]. When the depth of cut is of the same order or smaller than the tool tip radius, it has been shown that there are interactions which cause an increase in the specific force, force per unit volume of work material removed, required to cut the work material [11,12].
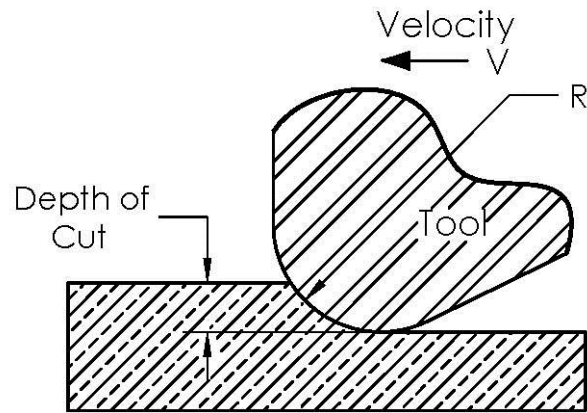
Figure 4: Note that the depth of cut and the tool tip radius are of a similar magnitude.

Experiments which have investigated this small depth of cut range have typically reported the forces of cutting or temperature increase while cutting. During one of the typical experiments, a bone sample is cut in a specific direction, based on the primary bone osteonal direction. During this event, the cutting forces and temperature rise of the sample is measured. These published works rarely, if at all, theorize to the root cause of the temperature rise. This thesis focuses on the following hypothesis: **elastic deformation during the cutting of bone, which does not contribute to chip formation, is a significant contributor to the energy required to cut. This degree of elastic deformation can be approximated by evaluating the energy absorbed during bone cutting.** It is assumed that there is a significant amount of elastic compression during the process of cutting bone, and it is this energy that is thought to account for the majority of heat generation during cutting. The effects due to this elastic deformation are theorized to be of greatest percentage at depths of cut on orders of magnitude where research is lacking, below 0.1 mm (.005").

To test this hypothesis, a set of experiments was conducted in which a saw tooth attached to a sliding carriage was allowed to transverse a constrained inclined plane. This saw tooth impacted a specific length of bone sample with a prescribed depth of cut. During this event, the position of the tool carriage was measured with a linear magnetic encoder, and the kinetic energy in this carriage was calculated from that data. These cutting experiments were compared to baseline data, where the tool did not impact any work piece, and the energy expended during the cutting of bone was extracted. Along with this kinetic energy measurement, the forces during the cutting event were measured using a three-component dynamometer. Comparing these two measurements allowed for the derivation of energy absorbed by the cutting event. This method of energy measurement has not previously been conducted, as typical bone cutting experiments measure only forces during cutting. This new method will provide insight into the bone-cutting process and the cutting energies involved.

It behooves people to quantify the amount of energy that is introduced into the bone system during cutting, as it allows for modifications of cutting practices in the operating room. The understanding of friction and elastic effects of bone cutting also allow for better use and design of tools for medical devices.

Background

Cutting of Metal

In order to draw conclusions relative to the cutting of bone, it is useful to study metal cutting models, as these models for metal cutting have been applied for many years.

The basis for most metal cutting models is the well-known Merchant's model of orthogonal cutting, as shown in Figure 5 [13].
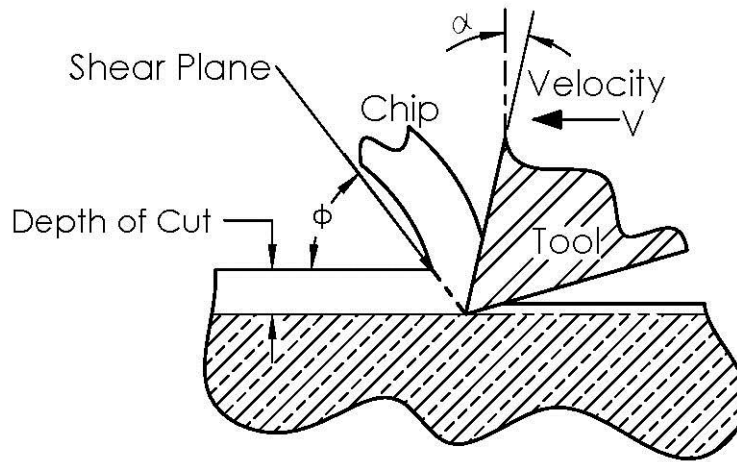
Figure 5: Orthogonal cutting as described by Merchant [13]

$$tan \, \emptyset = r_L \frac{cos \, \alpha}{(1 - r_L sin \, \alpha)}$$
(1)

$$r_L = \frac{t_1}{t_2}$$
(2)

$$t_1 = Depth \, of \, Cut; \, t_2 = Chip \, thickness$$

The orthogonal designation stems from the cutting edge of the tool being orthogonal to the direction of motion during cutting. This model utilizes several assumptions in order to reach the concluded equations for the forces of and work involved in cutting. As shown in Figure 5, the depth of cut is of a much larger order of magnitude than the cutting tool tip radius, meaning complex interactions at the tool tip can be omitted. Also, the assumption is made that all of the deformation during cutting is of the plastic type. Merchant assumes that the work material fails in shear along a specific shear plane, material dependent, described by Φ, which can be determined by the Merchant equations, (1)and (2). This model has been the basis for many experiments which

measured the forces in order to determine Φ. This has allowed the Merchant model to become a staple when discussing most cutting operations.

Several modifications have been made to the Merchant theory of cutting in order to provide a model that predicts, to a greater certainty, the experimental data. One of these is the research conducted by M. Bäker, in which the author tests Merchant's assumptions of perfectly plastic deformation and that the minimization of cutting energy is the criteria that determines the shear plane [14]. Bäker developed a Finite Element Analysis in which he limited the deformation and forced the chip to follow a certain shear angle. His results were that the perfectly plastic assumption seems to be applicable; however, the theory that the minimization of the work leads to the concluded shear angle is of question. The author then creates a system in which the work piece is directed to create a chip with a certain shear angle, using the Merchant assumptions. This analysis creates a chip that does not follow the Merchant shear angle theory, and he directs attention to the fact that the cutting force is larger than predicted by Merchant. This observation shows that the work of cutting may not be accurately predicted by Merchant. Bäker concludes that in order to further the study of chip formation, the calculation of shear angles of chip formation should be revisited.

Molinari and Moufki published a more recent theory that modifies several assumptions of the Merchant model in order to attempt to accurately predict the shear plane [15]. The authors initially mention that Merchant's assumption of a perfectly plastic material may be the root cause of this mismatch. However, upon calculating the minimum shear

angle using Zvorykin's Law, which uses constants obtained from experiments, it is shown

that this assumption is not the main cause. Using the result from Bäker, the authors

apply changes in the free surface geometry, along with Upper and Lower Bound theory

to calculate a modified shear angle, ϕ_{MM}, which results in a stable chip thickness and

minimum cutting energy. The final result of which is that ϕ_{MM} differs from $\phi_{Merchant}$ only

by an added term of θ/2, where θ depends of the free surface geometry, outlined in

Figure 6.
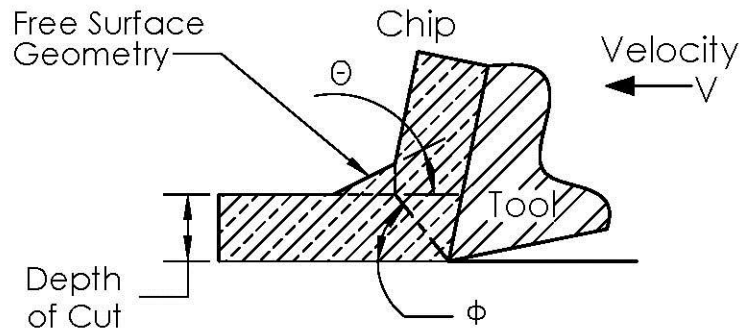
Figure 6: Modified orthogonal cutting as described by Molinari [15]

$$\phi_{MM} = \frac{\pi}{4} + \frac{\alpha - \theta - \lambda}{2}$$

(3)

$$\lambda = friction\ angle\ between\ tool\ and\ work\ piece$$

There is a large discrepancy in the Merchant model when the depth of cut is reduced so

that it is of the same order of magnitude as the tool tip radius. This orthogonal cutting

model does not apply at this scale, as shown by the non-linear increase in specific

cutting energy, detailed by Malak and Anderson discussed in later sections. During a

PhD dissertation, Thomas James proposes a different model that is applicable to this

depth of cut scale [16].
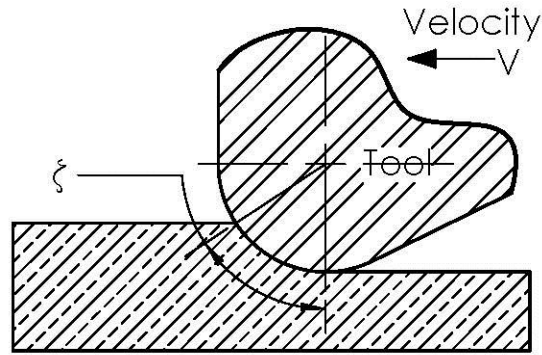
Figure 7: Work piece rolling under tool as described by James [16]

Using a Design of Experiments technique, James reaches several conclusions about the mechanics of this small depth of cut material removal that occurs during sawing. The main conclusion is that the removal can be described by the process of wear, in which the process of chip formation includes the ploughing of material. Using this wear and ploughing hypothesis, the author completes several experiments and compares them to a theoretical model. The results of this show that the computed model sufficiently predicts the effects of thrust force and blade speed on the cutting rate. However, this model does not predict a cutting force. This knowledge brings the effects of wear and ploughing in a sawing process to light.

Bone Structure

Bone is an anisotropic, non-homogenous material, the mechanical properties of which vary in discrete directions ,and, in addition, different regions of the skeleton are comprised of different bone structures.
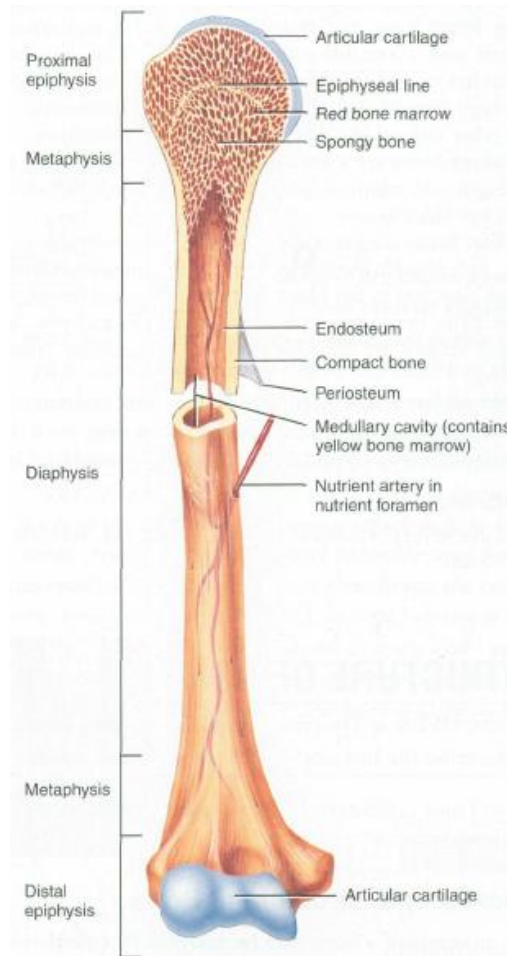
Figure 8: Macro scale long bone anatomy [17]

Figure 8 shows the macroscopic outline of a human long bone, which is composed of several main sections. The middle section of the bone is known as the diaphysis, which contains mostly compact or cortical bone. It is the stiffest section as it must support the loading of the human body. The proximal and distal ends of the bone are known as the epiphysis. This section is composed of a thin layer of compact bone on the outside, and the inside is composed of so-called spongy, or cancellous, bone. The mechanical function of the cancellous bone is to absorb the impact caused by movement during human motion; this cancellous bone is, essentially, a living damper. The third section of

bone is known as the metaphysis, which is the transitional section between the

epiphysis and the diaphysis.
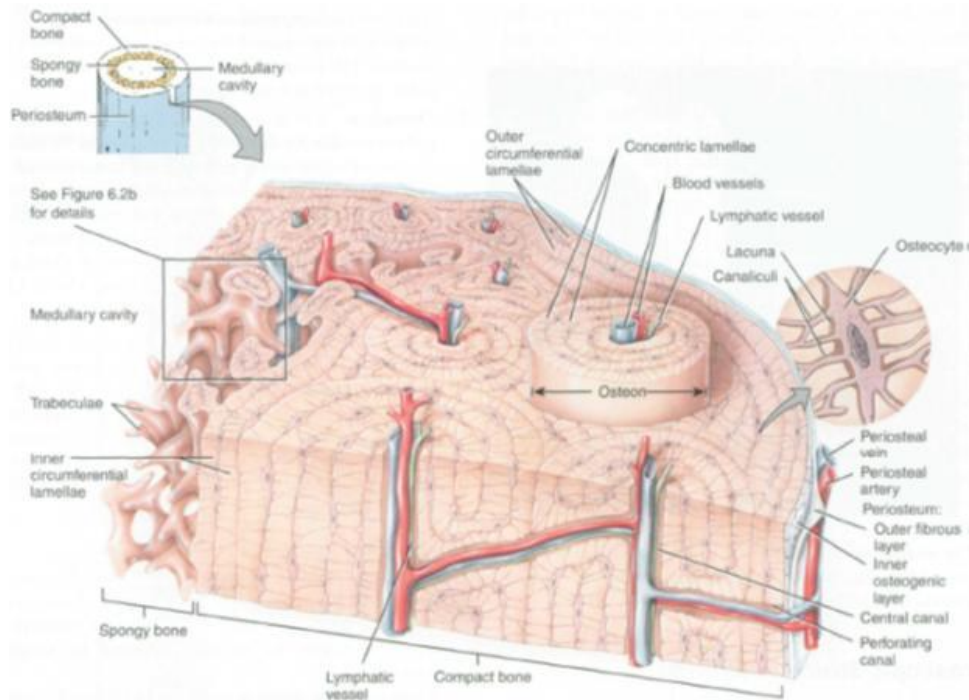
Figure 9: Micro scale of bone anatomy [17]

When examining the microscopic scale of bone composition, Figure 9, it is observed that

bone is a composite, directional material. The composite nature of this type of bone,

known as Haversian bone, stems from the composition of fibrous collagen which is

reinforced by calcium phosphate [18]. Composed of osteons and concentric lamellae

(calcified matrix), Haversian bone can be thought of as a number of stiff fibers, weaved

together to form a bone. These woven fibers are known as primary osteons, and are

generally oriented along the long axis of the bone. This anisotropic structure induces

material properties that are highly dependent on direction.

In bone, there are numerous inter-bone spaces; some are known as Haversian canals,

where blood and lymphatic vessels grow in order to bring nutrients to all parts of the

body [17]. When bone is subjected to a load, along any axis, these inter-bone spaces affect the compliance of the bone, and allow an elastic deformation of the system. In addition to the inter-bone space of these canals, bone is an inherently porous material. These pores typically contain fluids such as bone marrow. The stiffness of these pores is much less than the stiffness of the calcium, and this fluid effectively lowers the overall rigidity of the bone and increases local deformation upon loading [18]. The magnitude of bone deformation depends on numerous variables, principally the direction of the loading, whether it is applied radially, axially, or at some other angle relative to long axis of the bone. The anisotropy of the strength of bone, along with the inherent elastic deformation during loading, influences the amount of energy required to cut this structure.

Bone Properties

As this thesis deals with bone as a work material, it is necessary to review the mechanical properties of bone, which Natali and Meroi summarized in 1989 [19]. In order to review the state of biomechanical properties of bone, these authors decided to summarize the work completed so that they were able to standardize the mechanical properties of bone. In addition to the data presented in Table 1, the authors present a valuable analysis of stress versus strain as a function of the moisture level of the bone, completed by Knets and Melnis in a Russian journal. Their direction conventions are as follows: 1 is longitudinal, 2 is radial, and 3 is circumferential.

Table 1: Elastic constants for human bone summarized by Meroi [19]

	Reilly and Burnstein	Knets et al.	Katz	Ashman et al.	
E_1	11.5	6.91	18.1	12	(GPa)
E_2	11.5	8.51	19.4	13.4	(GPa)
E_3	17	18.4	26.5	20	(GPa)
G_{12}	3.6	2.41	7.22	4.53	(GPa)
G_{23}	3.28	3.56	8.65	5.61	(GPa)
G_{23}	3.28	4.91	8.67	6.23	(GPa)
v_{12}	0.58	0.488	0.285	0.376	
v_{13}	0.31	0.199	0.222	0.222	
v_{23}	0.31	0.142	0.207	0.235	
v_{21}	0.58	0.622	0.305	0.422	
v_{31}	0.46	0.315	0.325	0.371	
v_{32}	0.46	0.307	0.283	0.35	

Knets and Melnis presented their data at a symposium in 1999, in which they gathered

data from the diaphysis of male human tibias [20]. These tibia were subjected to

uniform tension tests at several strain rates and relative moisture contents. The results,

relative to moisture content, showed that there is a large dependence of the mechanical

properties of bone on the relative moisture content of the sample. For each level of

moisture content, several experiments were completed while varying the strain rate,

resulting in a comparison of the strength of bone relative to both variables. The most

prominent outcome when examining the moisture content is that the ultimate stress

varies as a result of moisture. Depending on the strain rate, the ultimate stress varies by

5 MPa, on average. Therefore, it is pertinent to ensure that any samples are of the same

moisture content when completing experiments with bone.

In order to apply new techniques and theories to the study of the mechanical properties of bone, Rho et al, completed a more recent review of the mechanical properties [21]. These authors' separated the testing and data gathered, based on the hierarchical structure of bone, macro, micro and nano-structures. Rho collects data from several sources, including his own previous work on cancellous and cortical bone, amassed through several different scales of measurement; this data is summarized in Table 2. This current thesis is related to the properties of the microstructure and macrostructure of bone as defined by Rho. The microstructure spans several osteons on the order of 10-500 µm, and the macrostructure is the combination of all of these osteons.

Table 2: Determining methods and values of elastic modulus of cancellous bone summarized by Rho [21]

Source	Test Method	Estimate of elastic modulus (GPa)
Wolff (1892)	Hypothesis	17-20
Runkle and Pugh (1975)	Buckling	8.69 ± 3.17 (dry)
Townsend et al. (1975)	Inelastic buckling	11.38 (wet)
Williams and Lewis (1982)	Finite Element model calculations	1.3
Ashman and Rho (1988)	Ultrasound	12.7 ± 2.0 (wet)
Ryan and Williams (1989)	Tensile testing	.76 ± .39
Hodgskinson et al. (1989)	Micro hardness	15 (estimate)
Kuhn et al. (1989)	Three-point bending	3.81 (wet)
Mente and Lewis (1989)	Cantilever bending with FEA	7.8 ± 5.4 (dry)
Choi et al. (1990)	Four-point bending	5.35 ± 1.36 (wet)
Rho et al. (1993)	Tensile	10.4 ± 3.5 (dry)
	Ultrasound	14.8 ± 1.4 (wet)
Rho et al. (1997)	Nano indentation	19.6 ± 3.5 (dry); longitudinal direction
		15.0 ± 3.0 (dry); transverse direction

A detailed analytical analysis of the porous microstructure of bone was undertaken by Sevostianov and Kachanov [22]. Using previously derived results from a separate Kachanov resource, the authors examine the impact of the size, shape, and densities of the pores within the structure of bone. In order to do this, the authors use a fourth rank tensor equation, in which the fourth rank tensor, H, is a cavity compliance tensor, used to model the compliance of the bone pores. This compliance is dependent on the volume of the pores, which, in turn, is dependent on the bone density of the sample. To completely estimate the elastic modulus, Sevostianov and Kachanov modeled bone as a composite composed of a collagen matrix with hydroxyapatite crystal reinforcement. The upshot of this research is the determination that the "presence of biological fluids (blood, lymph) and soft tissue (nerves, vessels) in the pores does not significantly affect the overall moduli" [22].

When examining the experiments of this thesis, a slight parallel can be made to the nano-indentation techniques for determining elastic constants, as the scales of energy required are similar. Using this nano-indentation technique, Zysset et al. measured the elastic properties at the lamellar scale [23]. The authors used a diamond nano-indenter and applied a Berkovich modified Boussinesq solution to calculate the modulus based on load and deformation:

$$\frac{dP}{dh} = \beta \frac{2}{\sqrt{\pi}} \sqrt{A} E_r \qquad (4)$$

Their conclusions of the elastic modulus of human cortical bone were 20.1 ± 5.4 GPa. However, upon further analysis, it seems that application of this model to the current thesis research is not appropriate, as the nano-indentation equation and assumptions

used are largely dependent on not spanning several lamellae. In the case of this thesis, the tool will be affecting a larger dimensional scale over several lamellae.

Mechanics of Bone Cutting

In bio-engineering, testing on biomaterials can be expensive and time-consuming. For example, to complete experiments on human bone, numerous safety requirements must be fulfilled, and a laboratory must be properly equipped. In order to prove the experiment procedure, a man-made test material is often substituted for the actual test material. In the case of human and/or bovine bone, a polyurethane foam block is typically the substitute. A classic substitute is an open-celled, polyurethane foam block, manufactured by Pacific Research Laboratories, known commercially as Sawbones. Since this is a typical starting point for bone property research, a study was completed by Malak and Anderson on the orthogonal cutting of this foam [24]. The authors conducted an orthogonal cutting experiment with this bone substitute while observing chip formation mechanics. The chip formation, which is applicable to this thesis, was what they referred to as a Type 1 chip, where the depth of cut was small, relative to the cell size of the foam. The chip formation process was described as "similar to the process of ploughing snow." The data gathered by the authors showed a prominent relationship between depth of cut and what they call specific cutting energy, energy consumed per unit volume of material removed. As the depth of cut decreased, this specific cutting energy actually increased non-linearly, directly related to their observation that it is similar to ploughing. This bone substitute is only that, a substitute, and in order to further the understanding of bone machining properties, actual studies

on bone must be considered to determine if this substitute accurately portrays the bone sawing process.

One of the first forays into the world of bone cutting mechanics was completed by William Krause in a PhD. dissertation in 1976 [25]. Krause, using bovine femur bone, examined the impact that many factors have on the cutting forces, including feed rates and tool rake angles. The first belief was that the Merchant theory of orthogonal cutting would apply, however, after analysis of the authors' data, it was shown to have limited applicability. According to Krause, the largest discrepancy between Merchant's theory and experimental bone cutting was a result of the Merchant assumptions of homogenous, isotropic, and ductile material properties. Bone is essentially the opposite of these assumptions, making the predictions of cutting forces inaccurate. The Merchant analysis is shown to be applicable in predicting the force, velocity, and work relationships while cutting, due to the fact that they are simply geometrically based, not material based. Krause brought to light the issues with the Merchant analysis on bone cutting and suggested further research be completed for a theoretical analysis.

Once Malak and Anderson completed their foam study, the authors began to delve into the world of bone cutting, where they researched the orthogonal cutting of cancellous bone [11]. The authors completed a series of orthogonal cutting tests and varied the depth of cut, the geometry of the tool, and the donor site of the bone. Referencing the previously undertaken polyurethane foam study, the authors noted several types of chips from the machining of their bone samples. In the femur, a discontinuous chip was

obtained for all cuts with a depth of cut smaller than 500µm (0.0197"). This type of chip was noted as a Type 1 chip in the previously discussed research, and again, the means of production is similar to ploughing snow. The authors discuss the specific cutting energy during this process, which is defined as the energy expended to remove a volume of material:

$$u = \frac{F_x}{wd} \qquad (\,5\,)$$

The authors observed that as the depth of cut was reduced, decreasing the volume of material removed, the specific cutting energy increased non-linearly. The experiments used a depth of cut that ranged from 0.1mm-2.0mm (0.004"-0.079") with increments of 0.1mm (0.004") below 2.0mm (0.079"), and .2mm (0.008") above 2.0mm (0.079"). This region of large values of specific cutting energy, along with the mechanisms behind it, is the region of interest for this current thesis.

A further study of bone machining characteristics was completed by Wiggins and Malkin, which focused on varying tool geometry in order to minimize cutting forces [12]. This study was experimental, in which the authors created a set up to follow the structure of orthogonal cutting and used it to measure forces during the cutting of bone. The authors also observed types of chip formation during this cutting, and, using micrographs, they observed fracture characteristics of the cutting process. The chips observed were formed by a fracture process and resulted in discontinuous chips, when cutting along the long axis of the bone. These authors generalized a model of chip formation where the bone fractures along osteonal boundaries as the tool moves into the work piece. The data gathered by these authors again shows an increase in specific

cutting energy required as the depth of cut decreases. This verification of the increase in specific cutting energy proves that the small depth of cut region needs to be researched to a greater extent. The authors completed these experiments in both bovine and human bone in order to draw conclusions between the cutting characteristics of both types of bone. Upon completion of the experiments, it was shown that the mechanics of chip formation is similar between both bovine and human bone, and similar cutting energy results were obtained. It is due to this knowledge that bovine bone will be used to complete experiments for this thesis.

Further research into the ploughing method of bone cutting was completed by Jackson, Robinson et al, who examined the micro-machining characteristics of bone at high speeds [26]. The authors proposed a model of chip formation and curl for micro-machining with depths of cut between 50-100 μm (0.0019-0.0039"), in which lamellae of the bone shears along the boundary to other lamellae. As these lamellar boundaries are not typically parallel, the outcome is a chip that is segmented and has a continuous curl. Their model of chip production was based on the Merchant model, and the authors concluded that it was applicable to the high speed, micro-scale machining completed. In the case of this thesis, the machining will be completed at a low speed, and therefore, a model of indentation or ploughing may apply with more accuracy.

Indentation/Ploughing

In 1960, P. Albrecht presented a paper that described the metal cutting model of ploughing using both theoretical analysis and experimental comparison [27].
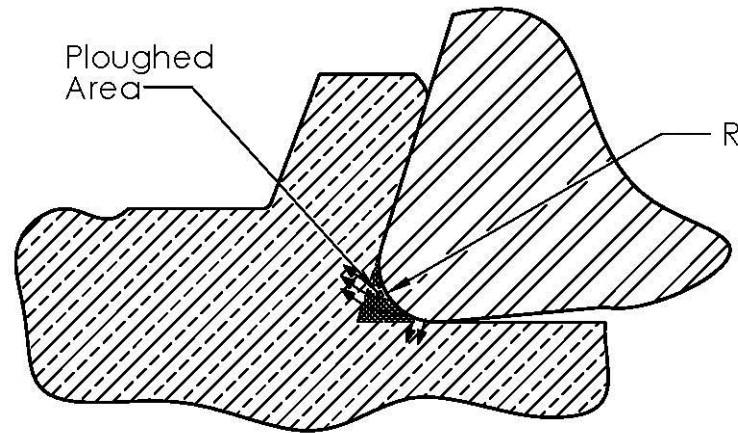
Figure 10: Flow of material during ploughing as described by Albrecht [27]

The author describes ploughing, which occurs in all cutting as the tool tip always has a radius. This is demonstrated in Figure 10 above, where the area in front of the rounded tool tip does not simply shear along the shear plane but is pushed or "ploughed" in the direction of the chip. There is not a simple one-direction force from this type of cutting, but rather, the force becomes the sum of the forces due to pressure across this rounded tool tip. The material is mainly forced upwards into the chip which is expelled from the work-piece, yet there is a small amount of material forced back into the work-piece which accounts for the residual compressive stresses in finished machined parts. The author then delved into a geometric analysis of this radius/work-piece interface and concluded that the sum of these forces can be represented by two forces. The first is a summation of the forces along the flat section of the tool, along which the chip travels upward. The second force is a single representation of the forces due to the pressures acting along the tip radius. Albrecht then geometrically reduced these forces to vectors that could be analyzed and compared to experimental results.

Following the summarization of his theoretical model, Albrecht discussed data gathered

from numerous experiments he completed [27]. Using a lathe, the author measured the

thrust and cutting forces for several different tool rake angles and depths of cut. These

results showed a non-linear relationship at very small depths of cut, where the ratio

between the uncut chip thickness and tool tip radius was largest. As this ratio became

smaller and the tool tip radius was no longer of great importance, the relationship

between the forces and chip thickness became linear. When the two forces were

plotted, thrust vs. cutting, while varying chip thickness, the relationship between the

forces was shown to be non-linear, at low depths of cut. The author reduced the cause

of this to the ploughing force being affected by the chip thickness until a certain depth

was reached where the ploughing force became fully developed. This cutting and thrust

force plot was also used by the author to determine the directions of the forces acting

along the tool faces, so that the ploughing model can be supported. Albrecht then

reviewed data gathered from an experiment where the same cutting was completed, for

several depths of cut, all while using cutting tools with specific tip radii, manufactured

by the lapping process. This data was used to verify the geometry of the cutting forces

predicted by the proposed model. Since this data reasonably matched the model

predicted forces, the conclusion was made that the proposed model is one that can be

used for future evaluations of cutting parameters and forces. Further experimentation

completed included investigation into the effect of cutting velocity and the relation of

ploughing to the curl of the chip. The studies of Albrecht form a foundation for the

understanding of ploughing; however, due to its age, the availability of new

technologies, and questions many have had about his conclusions, other articles must be consulted.

An in-depth model and experimental analysis was completed by a group at the University of Illinois, published in 1999. These authors analyzed two separate models of material flow during the ploughing of aluminum, the first of which models the material flow with a specific separation point on the rounded edge of the tool tip [28]. There is a specific point, S, on the tool tip, above which the material joins the chip created, and below which, the material is ploughed into the work-piece. The second model considered assumed that the tool maintained a built-up edge on the rounded tip of the tool. These two models of material flow are shown in Figure 11 and Figure 12.
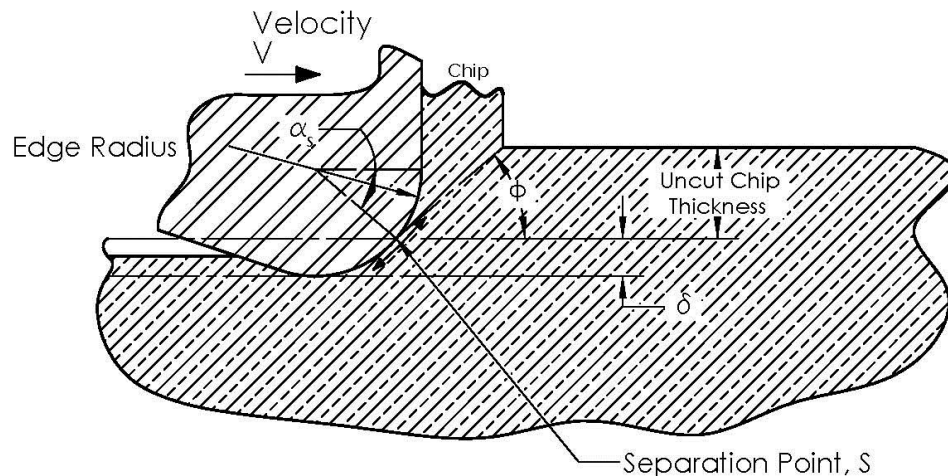
Figure 11: First flow model from Waldorf, for cylindrical indentation model. [28]
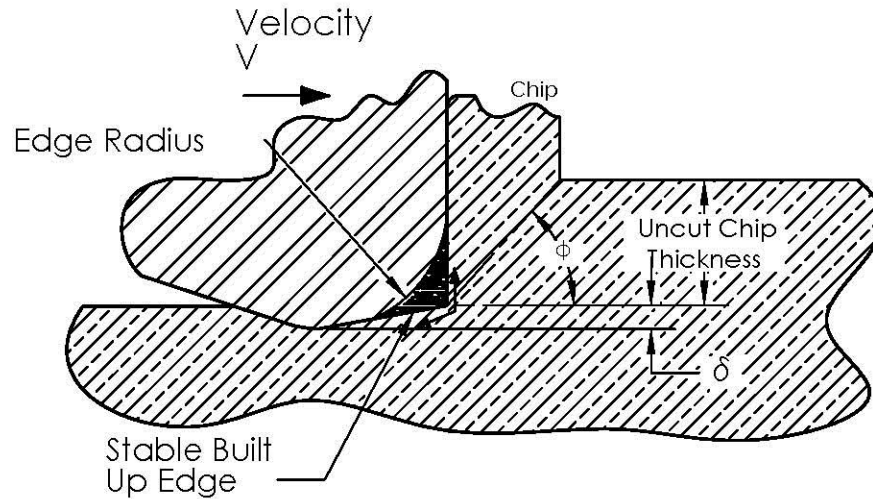
Figure 12: Second flow model from Waldorf, built up edge for blunt indentation. [28]

In consideration of the first flow model, the authors hypothesize that the forces can be predicted by using a modified cylindrical indentation model with modifications to account for the "indenter" sliding along the work-piece surface. Based on Figure 11, the indentation model is an appropriate choice for the modeling of these cutting/ploughing forces. When calculating the shearing component of the forces, the authors used a shear plane from the separation point, S, to the free surface of the work-piece, calculating the shear angle using their described equation (3). In order to determine the ploughing components of the cutting forces, the authors use the previously mentioned indentation model of a long rigid cylinder. In addition to the indentation component, the authors apply a sliding cylinder analysis to this model to eventually reach a prediction for the forces relative to ploughing the material.

In the case of the second model, the built-up edge, the theory of blunt indentation is applied to the cutting of aluminum due to the relatively flat surface of the built-up edge that is indenting the work-piece, as shown in Figure 12. This blunt indentation is

29

combined with a sliding model to, again, produce equations for the forces of cutting in both the shearing and ploughing components. The shearing components are assumed to act on a single slip line, where the angle is computed with an equation from the Merchant analysis. Using these two separate models of cutting, the authors performed cutting experiments to compare the measured forces due to cutting to the modeled cutting forces. During these orthogonal cutting experiments, the authors observed that the work-piece material never came into contact with the clearance face of the tool, meaning the elastic deformation of the work-piece was small. The main variation during these machining experiments was the radius of the tool-tip, where small and large radii were used. The small-tip radius experiments were used to estimate the material flow stress in order to apply to the analytical models. The large tip radius experiments were used to validate the computed analytical forces. In the estimation of the shearing and ploughing components, the assumption was made that the ploughing components were to be the "difference between the estimated shearing forces and the measured forces," essentially making any error part of the ploughing forces.

When comparing the measured forces to the first model, the point of separation model, the authors noted that there was a general error of roughly 50%, and the actual trends differ from the predicted trends. The error when comparing the second model, the one of a built-up edge, was much smaller, and was roughly 15%. This model also accurately predicted the trends of the actual cutting forces, which they detail in several charts. The authors concluded that the forces due to ploughing of the material increase as the depth of cut increases, up until a certain point, where the ploughing forces settle and

stay constant. While these authors do not specifically investigate this transition depth,

several others have. As these predictions have a marked error, other ploughing models

will be investigated for application.

Basuray et al. investigated the specific transition depth between ploughing and chip

generation as an investigation into the angle of this neutral point [29]. Using a cylindrical

tool model and a built-up edge ploughing assumption, the authors calculated a specific

angle, relative to the work-piece face and cylinder center, where the machining

transitions from ploughing to chip generation. The angle was calculated to be 37.6^0. In

order to validate the model's analytical angle, an experiment was performed where a

tool was moved into a slightly inclined work-piece, as shown in Figure 13.
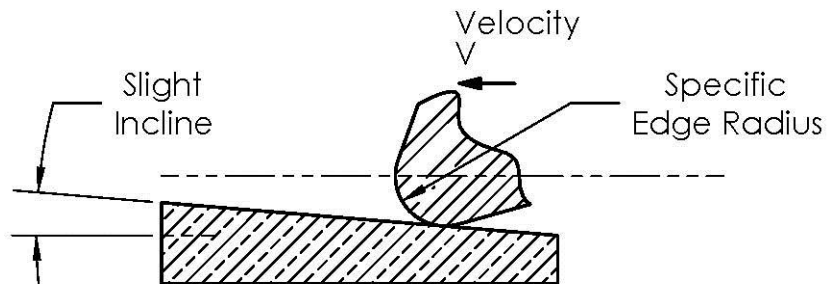
Figure 13: Diagram of cutting experiment from Basuray [29]

The tool was advanced into the work-piece until a chip was seen, and the system was

stopped. The depth of this specific cut was then measured. The data gathered allowed

the authors to calculate the value of the transition angle to be between 28^0 and 30^0.

Their data also showed that there was no relationship between the edge radius of the

tool and this so-called neutral angle, as they tested several tool edge radii. In response

to Basuray's experiment, several comments were made by Moneim [30], who criticized

the original author's choice of simplification to a small cylindrical model. In response to

31

the concerns of Moneim, it was shown that Basuray et al. understood that their model was only an approximate solution.

In November of 2010, Jun et al. presented research on a model for micro end milling, and while the model was developed for metal cutting, it applies the previously discussed principles of ploughing and shearing [31] and can be adapted to this thesis. The authors present two cutting models for the situation where the depth of cut was of the same order or smaller than the tool-tip radius. The two cutting models are depth of cut dependent, and there is a specific depth of cut where the cutting transitions from the so-called ploughing dominant regime to the shearing dominant regime.
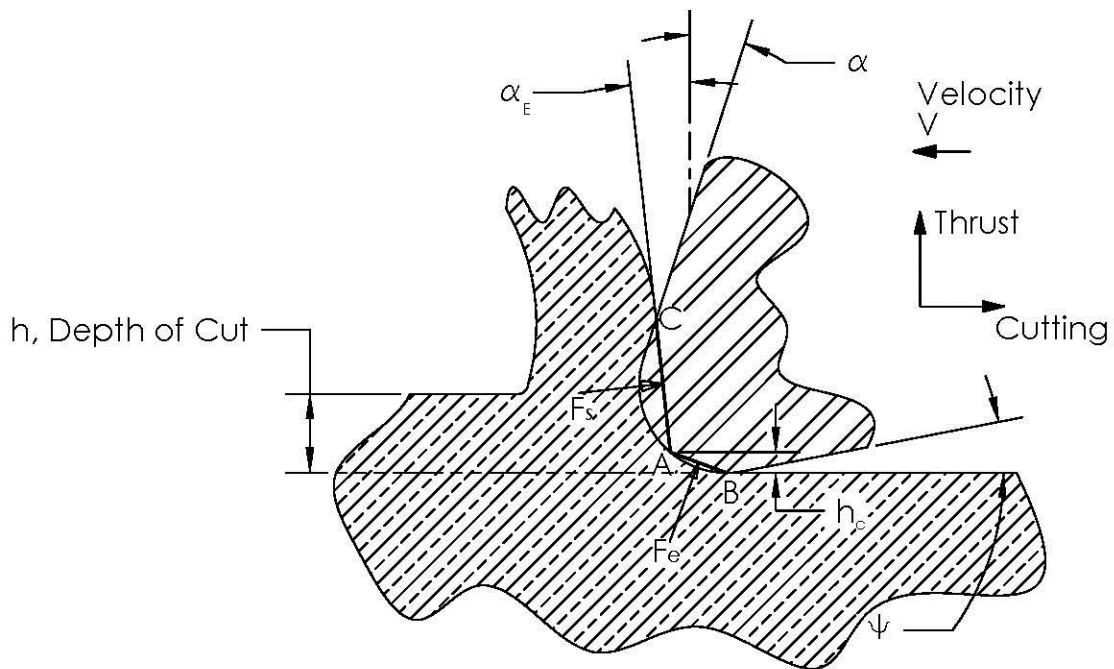
Figure 14: Shearing dominant regime according to Jun. [31]

The first model, the shearing dominant regime outlined in Figure 14, is a chip formation and cutting model applicable when the depth of cut is large enough to allow for chip

formation. The authors divided the face of the tool into two sections, segments AC and AB. The point A is the point at the "height of the minimum chip thickness" or the separation point according to Waldorf [28]. The forces that act on section AC are shearing dominant forces, in a normal direction and a frictional direction on the face. The forces acting on section AB are due to ploughing and are shown as normal and friction ploughing. Converting the rotational models of the authors to an orthogonal coordinate system of cutting and thrust directions, the equations of the forces become:

$$F_{CS} = h(K_{NS} \cos \alpha_E + K_{FS} \sin \alpha_E) \qquad (6)$$

$$F_{TS} = h(-K_{NS} \sin \alpha_E + K_{FS} \cos \alpha_E) \qquad (7)$$

Where h is the depth of cut, α_E is the effective rake angle of the face, and the K constants are the specific cutting energies or cutting coefficients for the particular direction of the shearing dominant regime. The authors compute the effective rake angle by averaging the instantaneous rake angles along the tool-tip radius using an integral.

The second model developed by Jun et al. is for the region where ploughing dominates the model of cutting, where the depth of cut is smaller than the minimum chip thickness, and no chip is generated as outlined in Figure 15.

33
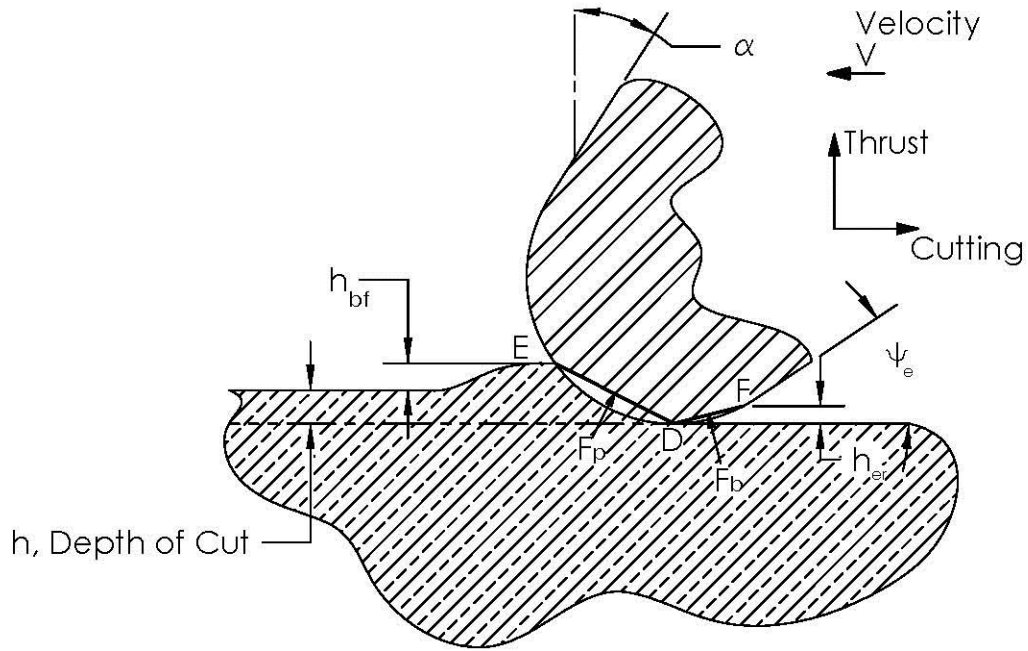
Figure 15: Ploughing dominant regime according to Jun. [31]

This ploughing model, again, separates the tool tip into two regions, DE and DF. In the

work-piece, there is the interesting effect of a pile up in front of the tool, described by

h_{BF}. There is also a region of elastic recovery on the rear face of the tool, described by

h_{ER}. The forces on face DE are due to the ploughing of the piled up region, which can be

represented by using geometric parameters from a standard scratch test model, while

the forces on the face DF are resultant from the rubbing of the material that has

recovered from elastic compression. The forces in this ploughing dominant regime, in

the cutting and thrust directions, are:

$$F_{CB} = h_{ER}(-K_{NB}\sin\Psi_E + K_{FB}\cos\Psi_E) \qquad (8)$$

$$F_{TB} = h_{ER}(K_{NB}\cos\Psi_E + K_{FB}\sin\Psi_E) \qquad (9)$$

In these equations, the K constants are, again, specific cutting energies or cutting

coefficients in the particular directions for this particular cutting regime that are

determined experimentally.

34

It is this model, which details a specific changeover between two main models of cutting

at a specific depth of cut that is of great interest to this thesis. After proposing their

cutting model, the authors pursued a set of experiments in which, essentially, the depth

of cut was varied, allowing them to validate both the ploughing dominant and shearing

dominant models. The analysis of their data concluded that at low-feed rates, ploughing

and rubbing forces are significant contributors to the overall cutting force, and the tool

edge radius has a large effect on these forces. Due to the numerous similarities between

this model and a sawing process, this micro-milling cutting model will be applied to the

bone sawing in this thesis.

Methodology

Fixture Design

To estimate the contribution of the energy of elastic deformation during bone cutting, a test fixture was designed and manufactured. The general design of this fixture was an adjustable inclined plane wherein the cutting tool traveled down and passed over the bone sample causing interference. The change in kinetic energy of the travelling mass due to the cutting of the bone, in addition to the forces of cutting, was measured.

Figure 16 shows the complete test fixture with important features labeled.
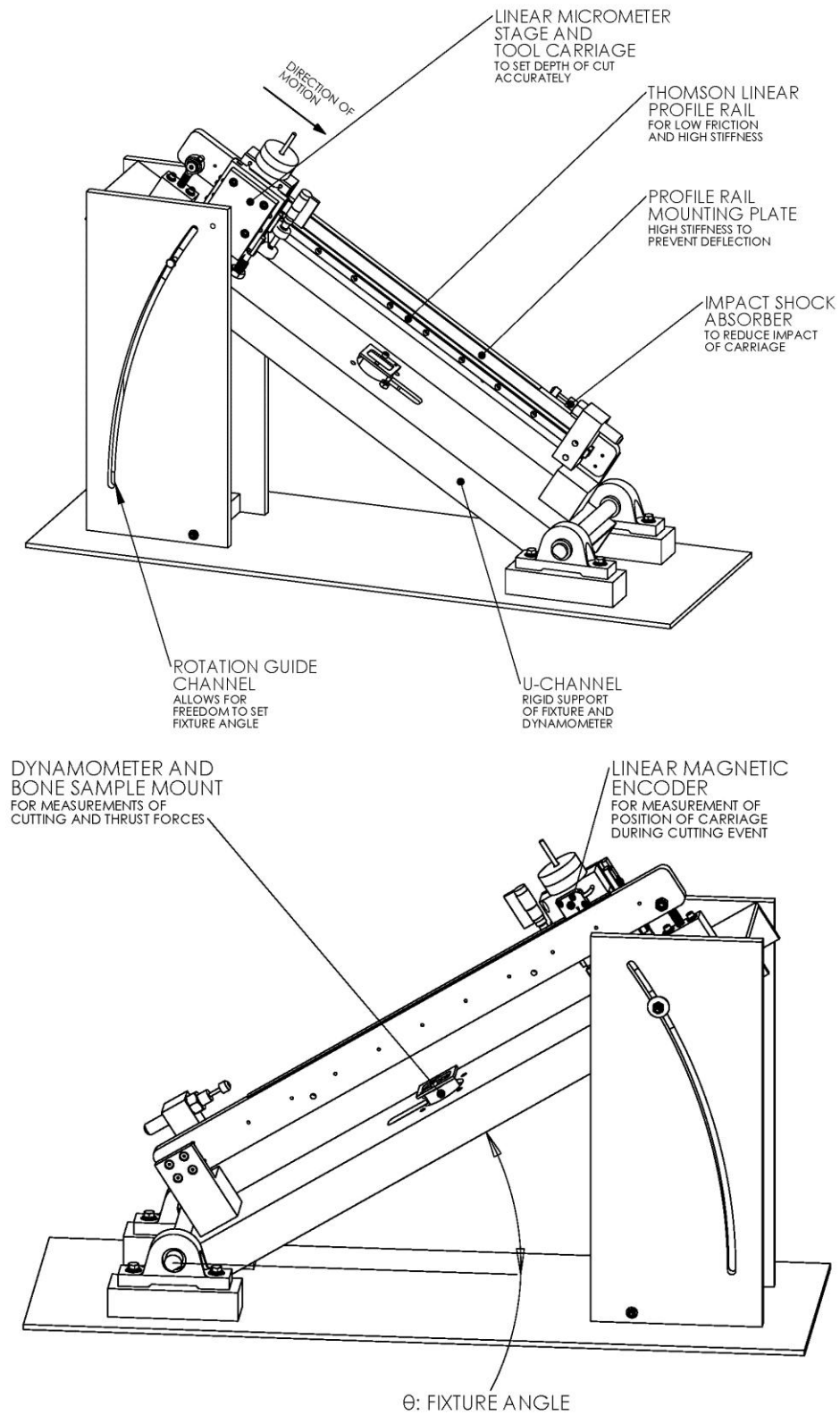
Figure 16: Testing fixture, highlighting specific features.

The fixture was designed to utilize a Thomson 500 Series Ball Profile Rail and Carriage, which was chosen for its quality, stiffness, and position accuracy, detailed in Figure 17 and Table 3.
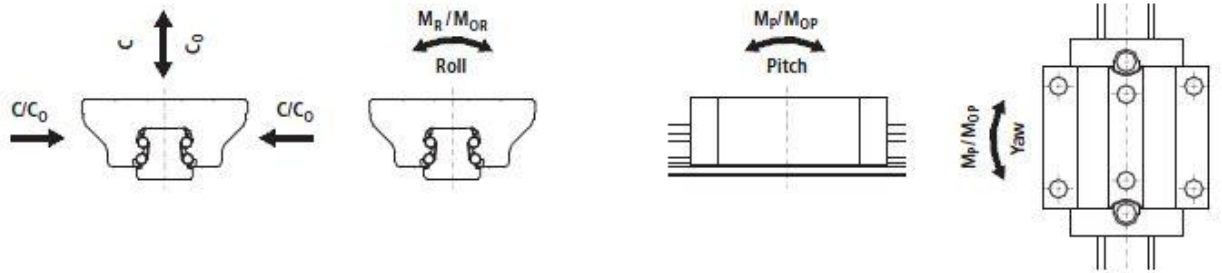
Figure 17: Load and moment conventions for Thomson 500 Series Ball Carriage [32]

Table 3: Thomson 500 Series Ball Carriage specifications [32]

	C Dynamic Load Rating	M_R Dynamic Moment Rating	$M_{P,Y}$ Dynamic Moment Rating	Maximum Velocity	Preload	Precision Class
Thomson 511U15A3 Carriage Characteristics	9000 N (2023 lbs.-force)	83 N-m (61.2 lb-Ft.)	67 N-m (49.4 lb-Ft.)	5 m/s (197 in/s)	.13*C=1170 N (263 lbs.-force)	Ultra-Precision

The maximum velocity of the tool carriage was calculated by assuming a maximum angle of 45^0 using a rail length of 600 mm, and neglecting friction, as shown in Figure 18.

$m = 4.5\ \text{KG}\ (10\ \text{LB})\ \text{MAX}$

$\theta = 45^0;\ L = 600\ \text{MM}$
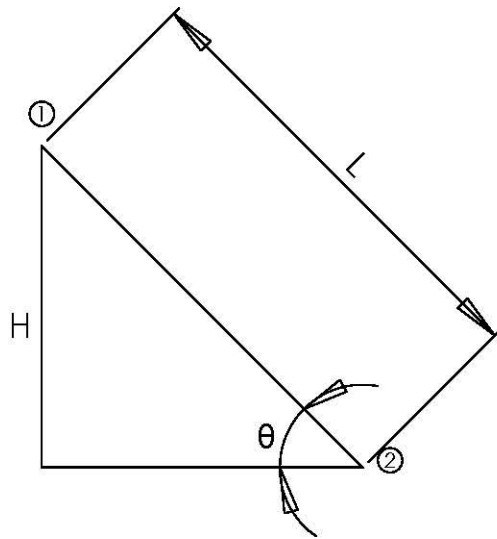
$H = L*SIN(\theta) = (600)*SIN(45)$
$\qquad\qquad = 424.26\ \text{MM}$

$KE_1 = 0;\ PE_1 = mgH;\ g = 9.81\dfrac{M}{S^2}$

$KE_2 = .5mV_2^2;\ PE_2 = 0$

DUE TO CONSERVATION OF ENERGY:

$PE_1 = KE_2$

$mgH = .5mV_2^2$

$V_2^2 = 2gH = 2(9.81)(.42426) = 8.324$

$V_2 = 2.885\ \text{M/S}$

Figure 18: Maximum velocity calculations

To provide ease of installation and use, the top face of the linear rail was mounted vertically, which required verification to ensure it did not exceed the dynamic yaw moment rating of 83 N-m (61.2 lb-Ft.).
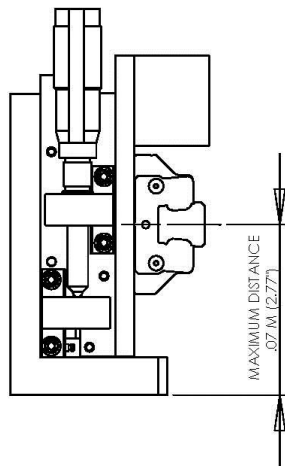
DYNAMIC YAW MOMENT RATING: 67 N-M

MOMENT = FORCE*DISTANCE

MAXIMUM FORCE ALLOWABLE:

$F = \dfrac{\text{MOMENT}}{\text{DISTANCE}}$

$F = \dfrac{67\ \text{N-M}}{.07\ \text{M}} = 951\ \text{N}\ (215\ \text{LB.})\ \text{MAX}$

Figure 19: Maximum allowable dynamic force calculation

This maximum cutting force is beyond the typical forces required to cut bone [11].

The linear rail mounting plate was analyzed to determine the maximum deformation due to the application of cutting forces at the mid-span of the assembly. Both the U-channel and linear rail/rail mounting plate were modeled as fully fixed beams to calculate the mid-span deformation.

FULLY FIXED BEAM DEFORMATION

$$\delta = \frac{PL^3}{192EI}$$

RAIL MOUNTING PLATE AND LINEAR PROFILE RAIL $I_{xx} = \frac{1}{12}bh^3 = 132609\ MM^4\ OR\ 1.33*10^{-7}M$

U-CHANNEL: $I_{xx} = 2452000\ MM^4\ OR\ 2.452*10^{-6}M$

RAIL MOUNTING PLATE AND LINEAR			
Load (N)	Deflection (M)	MM	INCHES
4.45	1.88E-07	1.88E-04	7.41E-06
8.9	3.76E-07	3.76E-04	1.48E-05
13.35	5.65E-07	5.65E-04	2.22E-05
17.8	7.53E-07	7.53E-04	2.96E-05
22.25	9.41E-07	9.41E-04	3.70E-05
26.7	1.13E-06	1.13E-03	4.45E-05
31.15	1.32E-06	1.32E-03	5.19E-05
35.6	1.51E-06	1.51E-03	5.93E-05
40.05	1.69E-06	1.69E-03	6.67E-05
44.5	1.88E-06	1.88E-03	7.41E-05

U-CHANNEL			
6061-T6 ALUMINUM E=70 GPA			
Load (N)	Deflection (M)	MM	INCHES
4.45	2.92E-08	2.92E-05	1.15E-06
8.9	5.83E-08	5.83E-05	2.30E-06
13.35	8.75E-08	8.75E-05	3.44E-06
17.8	1.17E-07	1.17E-04	4.59E-06
22.25	1.46E-07	1.46E-04	5.74E-06
26.7	1.75E-07	1.75E-04	6.89E-06
31.15	2.04E-07	2.04E-04	8.04E-06
35.6	2.33E-07	2.33E-04	9.19E-06
40.05	2.63E-07	2.63E-04	1.03E-05
44.5	2.92E-07	2.92E-04	1.15E-05

Figure 20: Deformation calculations for linear profile rail, and c-channel under cutting loads.

This maximum deformation of 0.002 mm (0.00008") under a load of 44.5 N (10 lb), which is more than double to typical cutting force for bone, provides sufficient stiffness so that there will be no measurable deformation of the fixture during experiments.

To accurately move the saw tooth during experimentation, a crossed-roller bearing linear stage from Newport Corporation was chosen for its load rating of 325 N (75 lb) and higher stiffness compared to a standard roller bearing stage. This linear stage featured a screw-lock, so the depth of cut was not affected by the cutting event. To

40

precisely increment the depth of cut during these experiments a Mitutoyo digital

micrometer, model 350-354-10, with accuracy of ± 2 μm (.0001") and resolution of .001

mm (.00005") was mounted to the linear stage. This resolution allowed for the accurate

setting of the depth of cut down to 1.27 μm (.00005"). This micrometer also included a

locking cam, so that it would not move during the cutting event.

As this thesis involves the measurement of instantaneous energy of the tool carriage, it

was necessary to determine a method to accurately measure the kinetic energy of the

carriage. Since energy is not easily measured directly, it was decided that energy would

be calculated by accurately measuring the position of the carriage over the cutting

event. With the position known, the instantaneous energy in the system was calculated

using the following equation:

$$V_i = \frac{\textit{Change in position}}{\textit{Change in time}} = \frac{\Delta x}{\Delta t}$$

$$KE_i = \frac{1}{2}mV_i^2 \qquad\qquad (10)$$

The tool carriage position was measured using a Renishaw LM10 linear magnetic

encoder system, which consisted of a read-head and a linear magnetic strip. This non-

contact position measuring tool was chosen based on its accuracy and frictionless

design, as this encoder had no influence on the energy of the system. An encoder was

purchased with an accuracy of 10 μm (.0004"), along with the Renishaw P201 USB

interface, which allowed for communication with the device along serial protocol, and

transferred the position of the encoder at a rate of 1 KHz. The encoder was mounted on

the testing fixture and calibrated using a 25.4 mm ±.0234 μm (1"± 1 μinch) Starrett

gauge block, allowing for accurate position data. To ensure proper alignment and

measurements, the linear magnetic scale and encoder were installed with great

precision following the outlined procedures in Renishaw installation documentation

[33,34].

In addition to energy during the cutting event, it was required to measure cutting forces

in the directions both normal and perpendicular to the movement of the carriage.
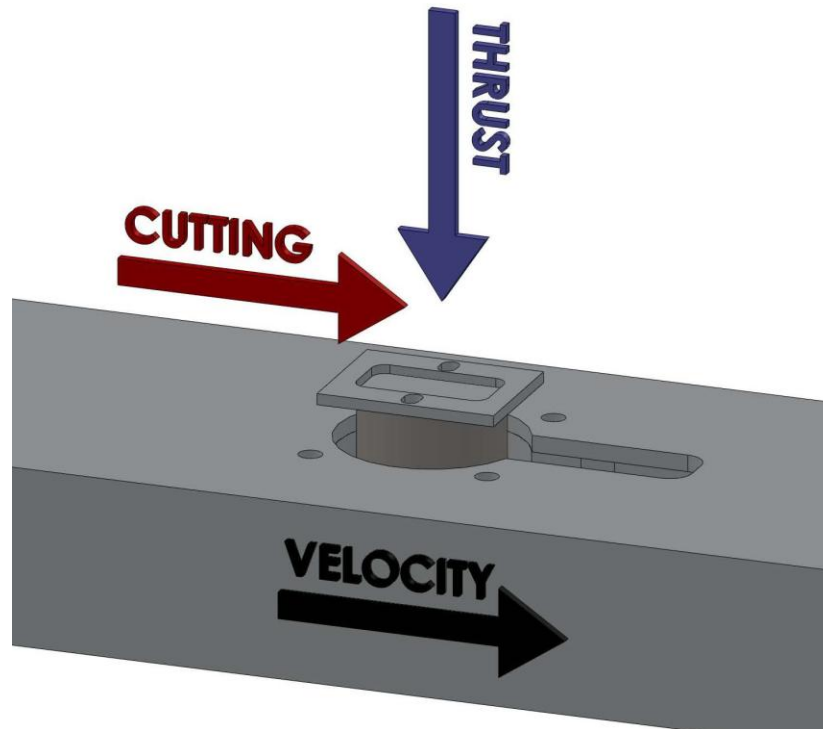
Figure 21: Thrust force and cutting force direction conventions

A Kistler 3-component force sensor (dynamometer) model 9047c was utilized to

measure the forces in the cutting and thrust directions. This force sensor was calibrated

by the ACLASS certified Kistler Instrument Corporation [35], using ANSI/NCSL Z540-1-

1994 and ISO/IEC 17025 standards. The result of this calibration was a sensitivity value

of pico-coulombs per pound that was utilized in the charge amplifier settings. This force

sensor was connected to a Model 5004 Dual Mode charge amplifier, which converted

the charge output from the dynamometer to a measurable voltage. The charge amplifier

was connected to a National Instruments BNC-2110 shielded connector block, which

passed data to a National Instruments PCI-6132 data acquisition board. This board was

able to collect data from an analog source, voltage, at a rate of 2.5 MHz per channel.

Cutting Direction

As was described previously, bone is an anisotropic directional material in which the

directionality of the primary osteons adds a specific variability to cutting bone. As a

result of this, there are three main directions that the bone can be cut, in relation to the

primary osteons, as shown in Figure 22.

Primary Osteons

(a)   (b)   (c)
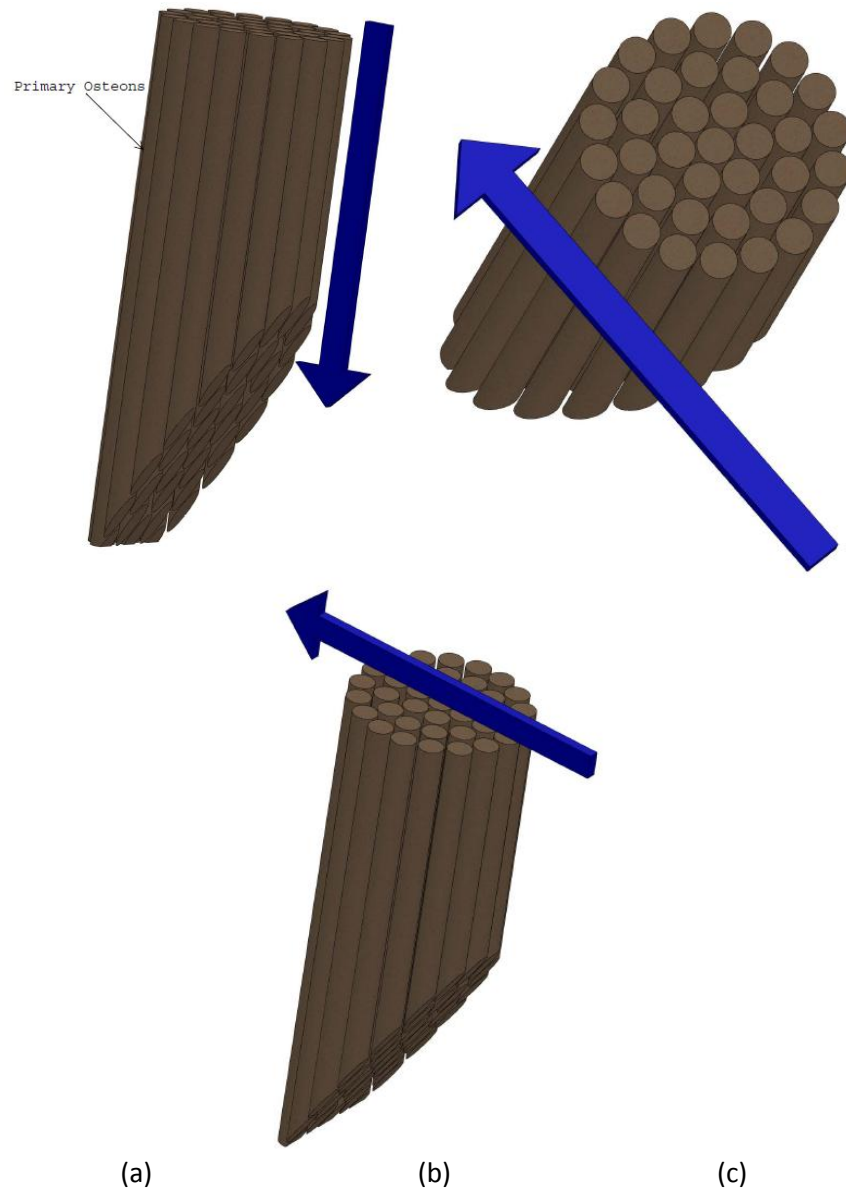
Figure 22: Cutting direction relative to primary osteon direction: (a) Parallel to primary osteons, selected cutting orientation. (b) Perpendicular to primary osteons. (c) Normal to primary osteons.

When cutting bone, both perpendicularly and normally to the primary osteon direction,

the tool travels over numerous osteonal boundaries, which results in sudden changes in

the cutting forces. Since the work and energy that is being measured in this experiment

is believed to be relatively small, these sudden changes would severely disrupt the

results. Therefore, the chosen cut direction for this experiment was parallel to the

primary osteons, Figure 22(a), minimizing the number of osteonal boundaries that are crossed during the cutting event, allowing for steady state cutting forces.

Sample Preparation

A local abattoir was visited in order to obtain bovine femurs from a slaughtered cow under 30 months of age [36]. This femur was flash frozen and kept frozen for 24 hours so that samples could easily be cut from the large bone.

Figure 23: Uncut bovine femurs

Using a Grizzly H6246 Meat Saw, the proximal and distal epiphyses were removed, and these bones were cut axially in half to produce two sections of bone. From this, two

38.1 mm (1.5") axial sections were removed from the raw bone. These two sections

were labeled, so the region the samples originated from could be identified.
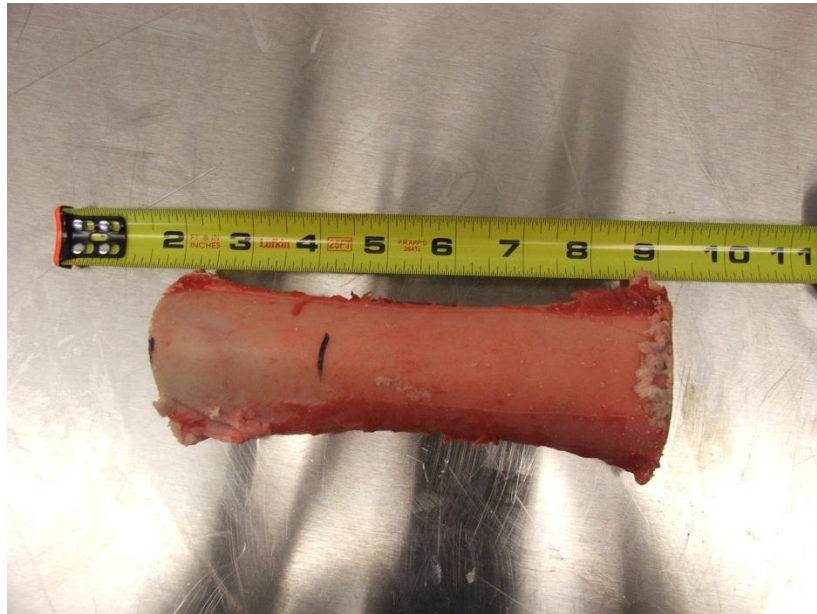
Figure 24: Bovine femur with proximal and distal epiphyses removed

Figure 25: Sections A and B of bovine femur, length of 38.1 mm (1.5"). Arrows indicate proximal end.

These two femur samples were then cut radially in order to maximize the production of

19 mm (.75") width samples, as shown in Figure 26 and Figure 27.
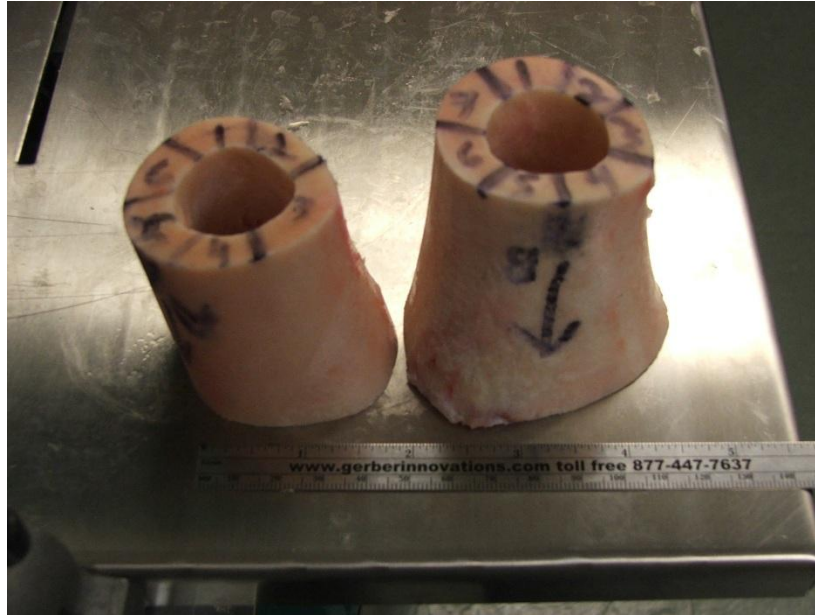
Figure 26: Bovine femur samples A and B, prior to radial sample cuts

Figure 27: Bovine femur sample A, subsequent to radial sample cut.

To maintain mechanical properties, the cut bovine bone was submerged in a 1X Hanks'

balanced salt solution (HBSS) when samples were not being produced. This Hanks'

solution is designed to maintain cell properties over time rather than promote growth.

Additionally, it is designed to maintain osmotic pressure and physiological pH so chemical and mechanical properties do not vary during storage [37].

To firmly attach the bone samples to the aluminum bone trays, 3M Marine Adhesive 5200 was utilized, due to its bond strength and resistance to salt water [38]. A layer of 5200 adhesive was dispensed into each bone tray pocket; each prepared bone sample was then pressed into this adhesive. The bone trays were labeled so that the samples could be distinguished from one another, and an absorbent towel soaked with HBSS was placed over the samples to keep the bone moist. Together, all of the samples were placed into a laboratory refrigerator to ensure that cells would not degrade due to rotting. The 5200 adhesive was allowed to cure for a minimum of 24 hours, while the absorbent towel was soaked in 12 hour intervals with HBSS to keep the samples moist.
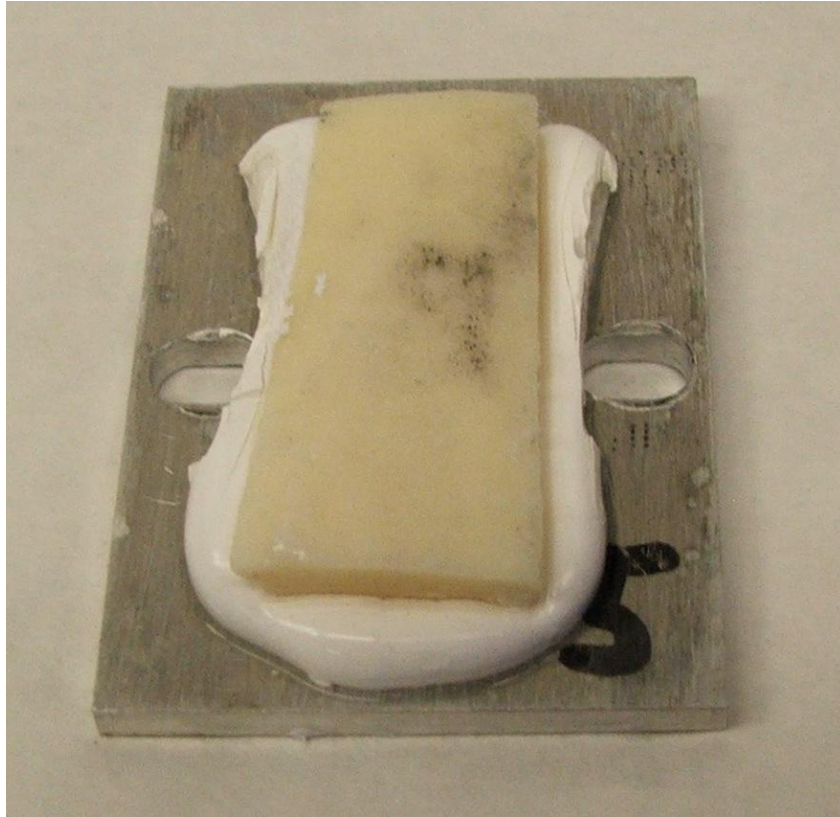
Figure 28: Bone sample mounted in bone tray pre-machining

To create a flat surface on which to begin the cutting experiments, the sufficiently cured bone samples were mounted to a machining jig on a Grizzly G0463 Mill machine. To keep the bone samples wet and to limit heat rise due to machining, the flat machining process was completed with the samples submerged under distilled water. Each sample was machined using a 13 mm (.5") diameter end mill until there was a consistent flat surface across the entire sample. Finished bone samples were submerged in HBSS to maintain mechanical properties.
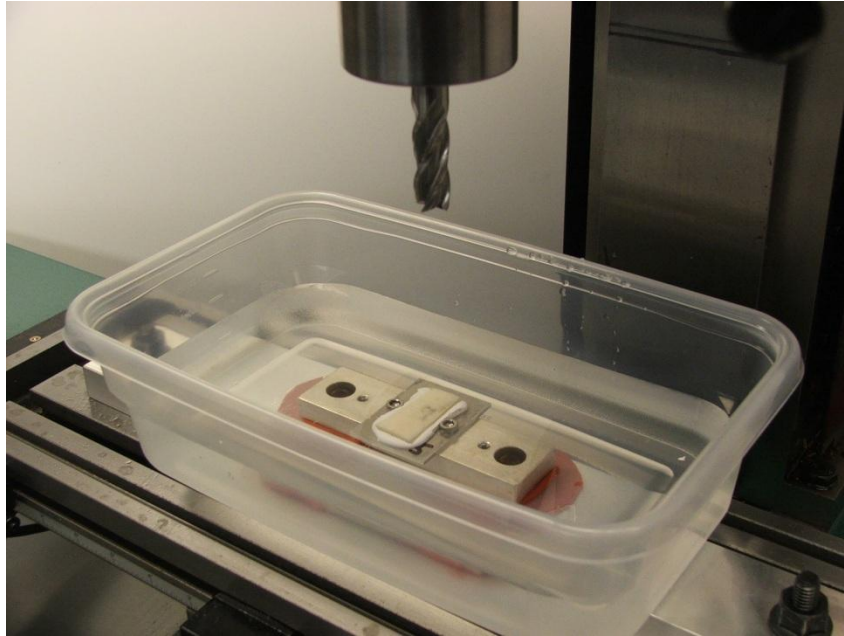
Figure 29: Bone machining sample fixture
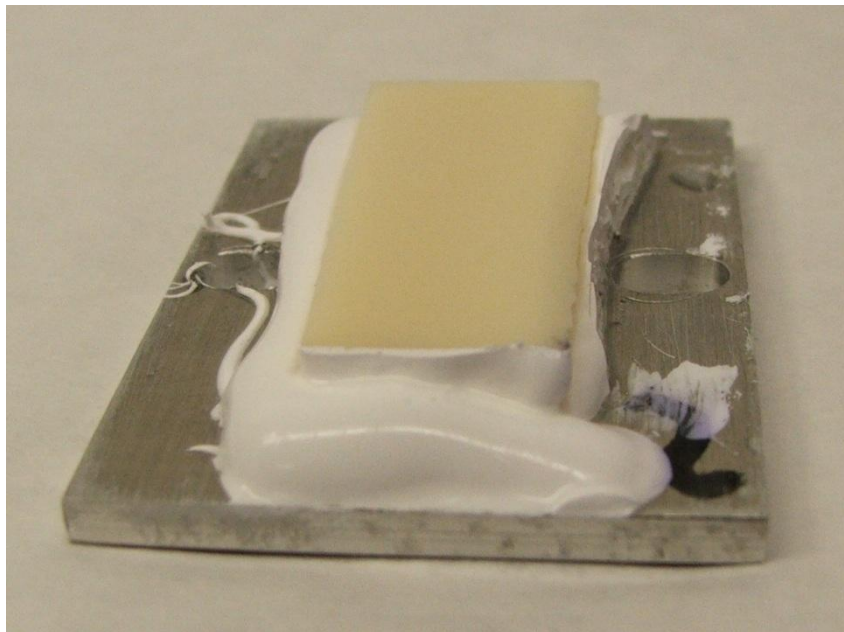
Figure 30: Bone sample in bone tray, post-machining

Fixture Preparation

The cutting tool chosen for this experimentation was a Brasseler reciprocating saw

blade, model KM-458.
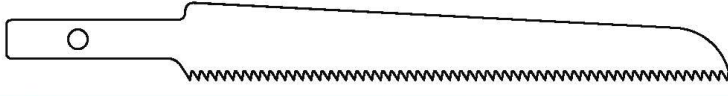
Order Number	Unit	Cut Depth	Cut Width	Material Thickness	Cut Thickness
KM-458	mm	89.00	12.50	0.60	1.00
	in	3.50	0.49	0.024	0.039

Figure 31: Brasseler USA reciprocating saw blade KM-458 profile [39]

These blades were cut with a Buehler Isomet 1000 Precision Diamond Saw into 9.5 mm

(.375") sections to allow mounting in the tool clamp. Subsequent to sectioning, the

blades were ground so that only one tooth remained in each section. Several teeth were

mounted in epoxy and then ground and polished to allow for the measurement of the

tip radius, seen in Figure 33.

Figure 32: Cut and ground Brasseler reciprocating saw tooth, arrow indicates cutting direction
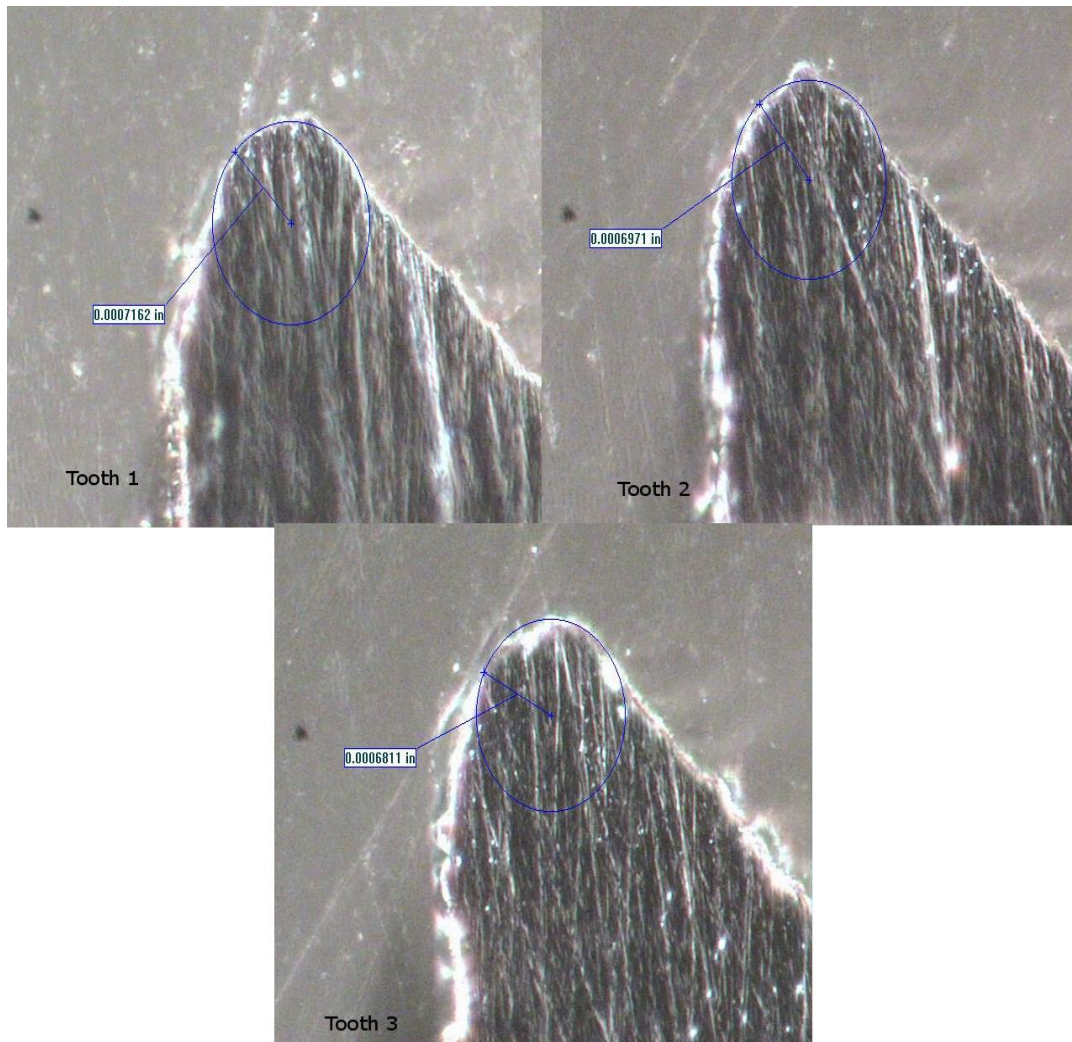
Figure 33: Sectioned, ground, and polished Brasseler blade teeth, at 100X magnification.

The average measured tooth tip radius was 17.78 μm (.0007"), a quantity that is larger than the depth of cut measured by Lannin and Kelley [9,10]. These blades were found to have a rake angle of 10°, measured by an optical microscope, as shown in Figure 34.
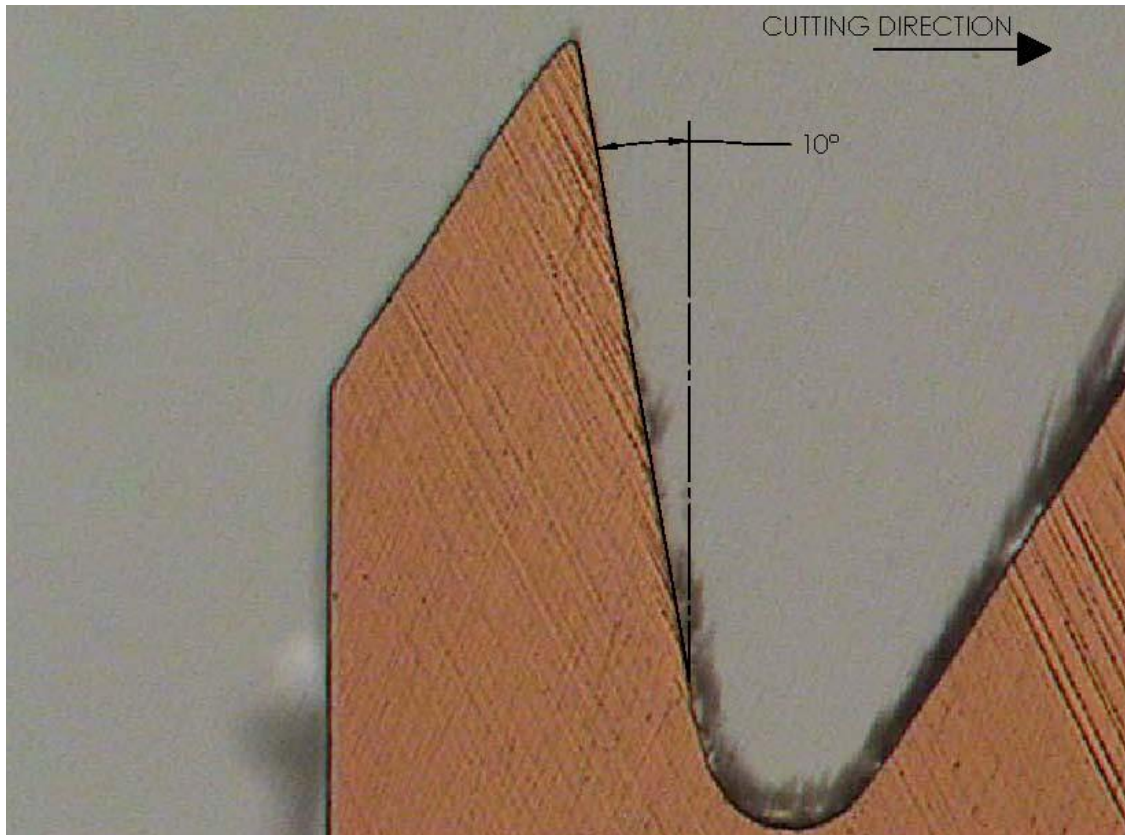
Figure 34: Brasseler tooth with measured rake angle (20X)

As the calculation for kinetic energy, Equation (10), requires the mass of the moving

object, the mass of the entire tool carriage was determined. Each of the carriage

components were weighed on a calibrated triple-beam balance to an accuracy of 0.1

grams, as outlined in Table 4.

Part Description	Mass [g]
Thomson Bearing	189.6
Encoder Mount/Encoder/Screws/Washers	270.1
Ground Aluminum Stage Mounting Plate/Screws	138.3
Newport Positioning Stage/Screws	580.4
Mitutoyo Micrometer	235.1
Tool Mount/Blade Clamp/Screws/Washers	387.6
Threaded Rod	19.4
Additional Circular Mass	194.0
Total Mass	**2014.5**

With the mass of the carriage specified, the other variable that has an impact on energy is the angle of the test fixture, as shown by calculations in Figure 35.

FROM WORK-ENERGY:

$$KE_1 - W_{1-2} = KE_2$$

$$W_{GRAV} = mgH$$

$$W_{FRICTION} = \mu mgCOS(\theta)$$

$$H = xSIN(\theta)$$

STARTS FROM REST; $KE_1 = 0$

$$0 + mgH - \mu mgCOS(\theta)x = \frac{1}{2}mV_2^2$$

$$g(xSIN(\theta)) - \mu gCOS(\theta)x = \frac{1}{2}V_2^2$$

$$V_2^2 = 2gx[SIN(\theta) - \mu COS(\theta)]$$
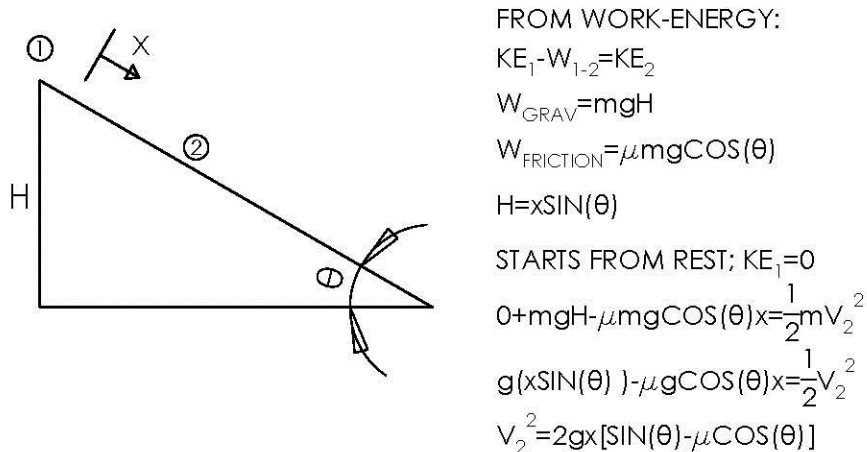
Figure 35: Calculation of theoretical instantaneous velocity

Using a Mitutoyo Digital Protractor Pro-360 with an accuracy of ±0.1°, a specific incline angle was chosen and set to prescribe an initial impact kinetic energy, velocity, at the

bone sample. A cutting tooth sectioned from the ground Brasseler blade was secured in the tool clamp with the specified rake angle leading in the cut direction.

Experimental Procedure

To begin the data sampling process, connect the Renishaw P201 Serial-to-USB converter to a computer with the LabVIEW programming base. Zero the encoder by moving the tool carriage above the starting pin on the test fixture and running the LabVIEW program "Zero_Encoder.vi." following the directions provided. Once the encoder has been zeroed and the bone tray has been mounted to the dynamometer, it is necessary to acquire a baseline profile for the tool carriage movement, without a cutting event. To do this, the LabVIEW program "Encoder_Data_Gather.vi" was used to acquire a minimum of 10 baseline position versus time profiles. During this entire process, it is necessary to keep the bone sample wet by spraying it with distilled water from a spray bottle. Again, this keeps the mechanical properties from degrading.

Prior to beginning actual experimentation, the surface of the bone sample must be made completely parallel to the rail, which was done by making a .025 mm depth (.001") cut across the surface of the bone. This ensured that the entire length of the sample was cut and that the cutting path was parallel to the rail. To gather data from the dynamometer, the LabVIEW program "Dyno_Data_Gather.vi" was utilized in conjunction with the encoder data gathering program previously mentioned. The micrometer was zeroed after the first pass to ensure parallelism to the rail, so the depth of cut could be incremented from a zero value.

To complete a single test run, first move the tool carriage above the starting pin. Set the depth of cut to the desired value and lock both the micrometer and positioning stage using the respective locks to ensure stability. Next, start both the dynamometer and encoder data sampling LabVIEW programs and pull the starting pin to initiate the cutting pass. Once the carriage has reached the bottom of the rail, stop both data sampling programs. Be sure to raise the micrometer depth to above the bone sample when resetting the tool carriage, so as not to damage the bone.

Data Analysis

As there are two separate data streams, there are two separate techniques required for the analysis of this data.

Encoder Data Analysis

The data gathered from the Renishaw encoder is of a hexadecimal format, and therefore, must be converted to decimal format prior to usage, which is completed by the LabVIEW program "Convert_Hex.vi." This converted data is then read into MATLAB by the script Renishaw_Data_Analysis.m." which converts the decimal strings to a distance measurement, along with calculating velocity and energy over the cutting event. This program also filters the data, using a MATLAB-generated, moving average algorithm to smooth the data provided by the encoder.
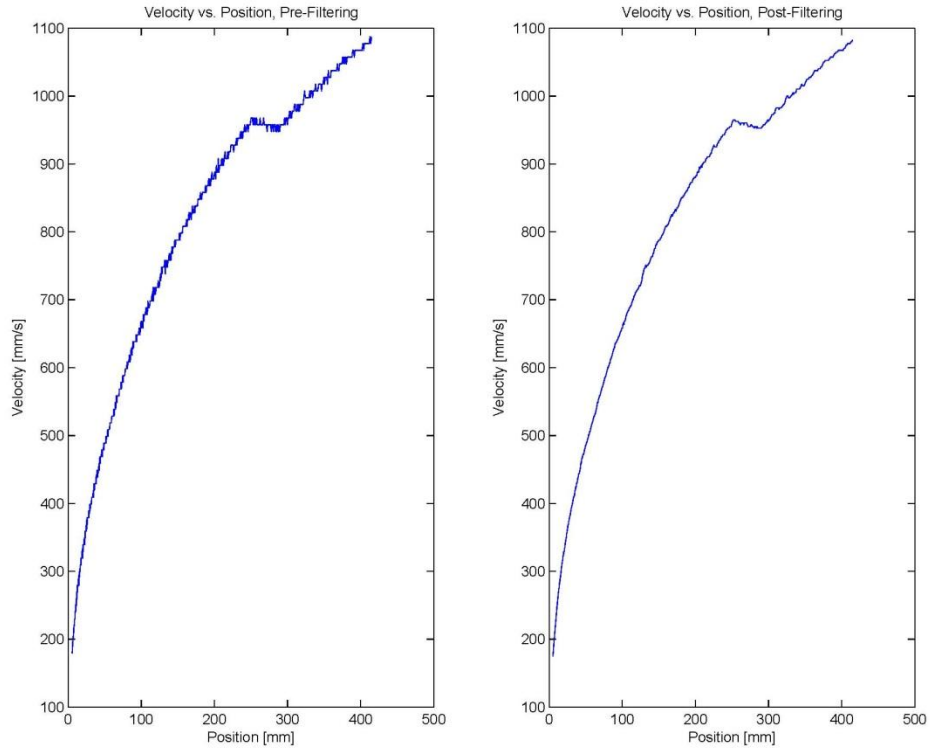
Figure 36: Computed velocity data, left: before applying described filter, right: after applying described filter

This filter was chosen as it was able to smooth the data without significantly changing the values, making analysis of this data acceptable. This filtered data is utilized in the MATLAB script "Get_Cut_data.m," a program which automatically crops the cutting event energy data so that final analysis is possible. This program compares the cutting event of each run to the associated baseline profile.
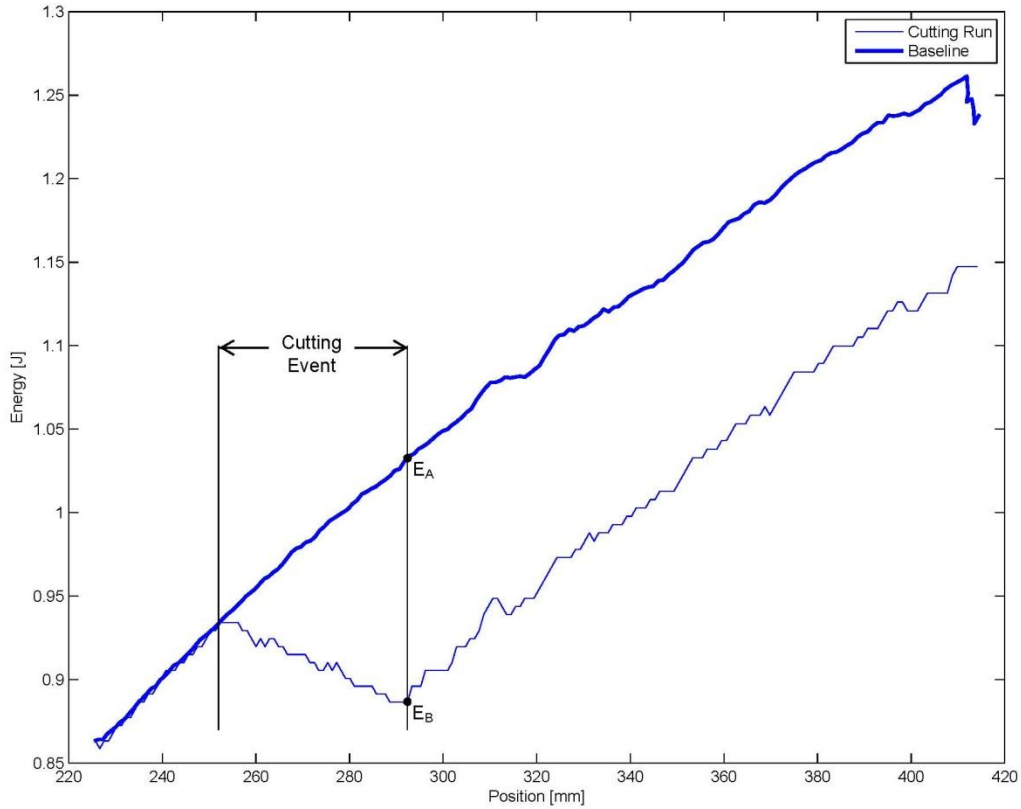
Figure 37: Comparison of cutting event energy vs. baseline energy profile

The energy value at the end of the cutting event was subtracted from the baseline run

to compute the energy lost in the specific cutting event, ΔKE.

$$\Delta KE = E_A - E_B \qquad (11)$$

Dynamometer Data Analysis

The data gathered from the Kistler dynamometer is a scaled voltage from -10 volts to

+10 volts, with 1 volt corresponding to 4.45 N (1 lb), due to the specified charge

amplifier settings. The LabVIEW data program generates a TDMS file type, which must

first be converted using the LabVIEW program "TDMSConvert.vi," to a comma-

separated values file type to utilize the data. This data was analyzed in MATLAB using

the program "Force_RMS.m," which reads in the data and allows the user to normalize

58

the data if there is a non-zero offset. The program then designs and applies a 4th order, low-pass, digital Butterworth filter, designed to filter out any high frequency resonance from the fixture vibration and smooth the data.
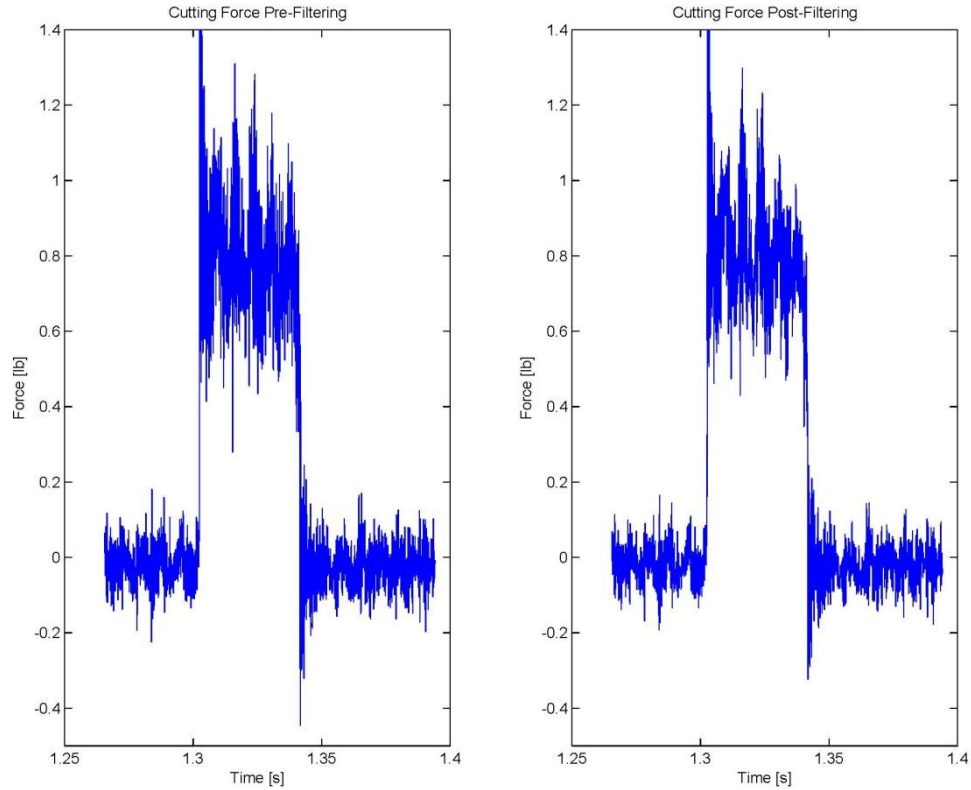
Figure 38: Cutting forces, left: before applying described Butterworth filter, right: subsequent to applying filter

The cutting event, as shown in Figure 38, was cropped and a root mean square (RMS) value was computed for both the cutting and thrust direction forces, F_C and F_T, in all cutting runs. Once both the encoder data and dynamometer data had been analyzed generating ΔKE, F_C and F_T, the raw data analysis was completed.

Design of Experiments

The experiments of this thesis were conducted using a Design of Experiments approach [40,41]. As this approach depends on the relationships between the variables (factors), screening experiments were completed detailing the effect of each input variable, carriage mass, fixture angle (referred to as initial cutting velocity), and depth of cut.

Mass Screening Experiments

A set of experiments was completed to show the relationship that the total tool carriage mass had on the energy absorbed during the cutting event. This was investigated due to the impact the carriage mass has on the initial carriage momentum. At a constant depth of cut, it was assumed that there would be no effect of the carriage mass on this energy absorbed during cutting. These experiments tested three different carriage masses at six depths of cut with a fixed fixture angle, θ, to maintain a constant initial velocity.

Table 5: Depths of cut and carriage masses for mass screening experiments

Depths of Cut [µm]	Depth of cut [in]	Carriage Mass [g]
1.27	0.00005	1820.5
2.54	0.0001	2014.5
5.08	0.0002	2208.5
7.62	0.0003	
10.16	0.0004	
12.70	0.0005	

Each carriage mass was made to cut at each depth of cut 11 times so that a statistically significant average could be reached. The data was analyzed and is summarized in Figure 39.
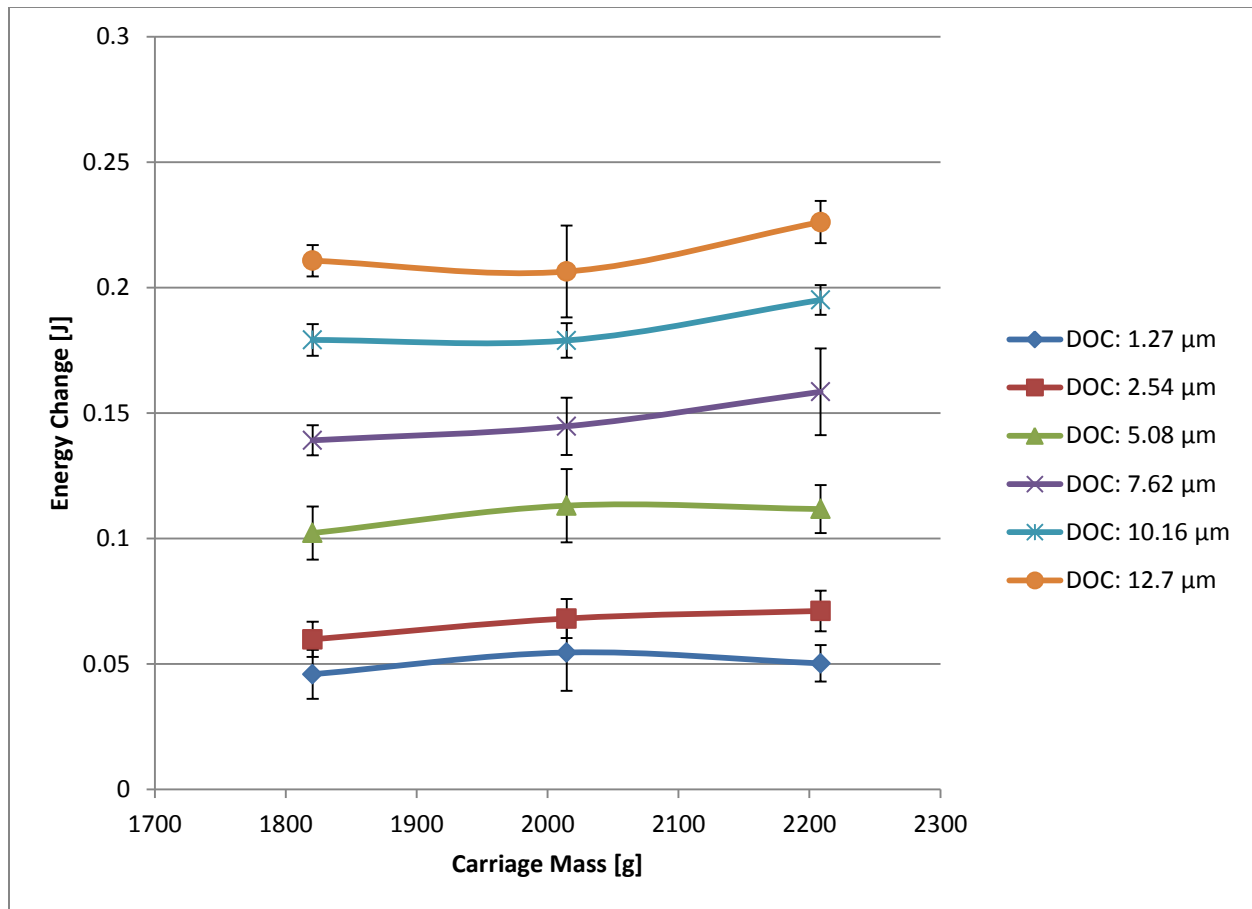
Figure 39: Effect of carriage mass on cutting energy at a constant initial cutting velocity

The data shows that the energy change due to cutting has no dependence on the carriage mass. The upshot of this result is that the mass of the carriage can be set to a specified value and is no longer considered a factor.

Initial Cutting Velocity Screening Experiments

As described in Figure 35, the incline angle of the fixture has an effect on the velocity of the carriage at the initial cutting instant. As such, it was necessary to find the relationship between the fixture angle, θ Figure 16 or initial cutting velocity, and the change in energy due to the cutting of bone. The initial cutting velocity screening experiments tested four separate initial cutting velocities at two depths of cut, outlined

in Table 6. As cutting research typically describes cutting velocity, the fixture angle will be referred to as the initial cutting velocity.

Table 6: Fixture angles, initial cutting velocities and depths of cut for initial cutting velocity experiments

Angle [Deg]	Initial Cutting Velocity [mm/s]	Initial Cutting Velocity [in/s]	Depth of Cut [μm]	Depth of Cut [in]
20	575	22.64	5.08	0.0002
25	780	30.71	7.62	0.0003
30	930	36.61		
35	1025	40.35		

Cutting experiments were run at both depths of cut for each of these four velocities with a minimum of 15 cuts each, allowing for a statistically significant average. The cutting energy data was collected and is displayed in Figure 40.
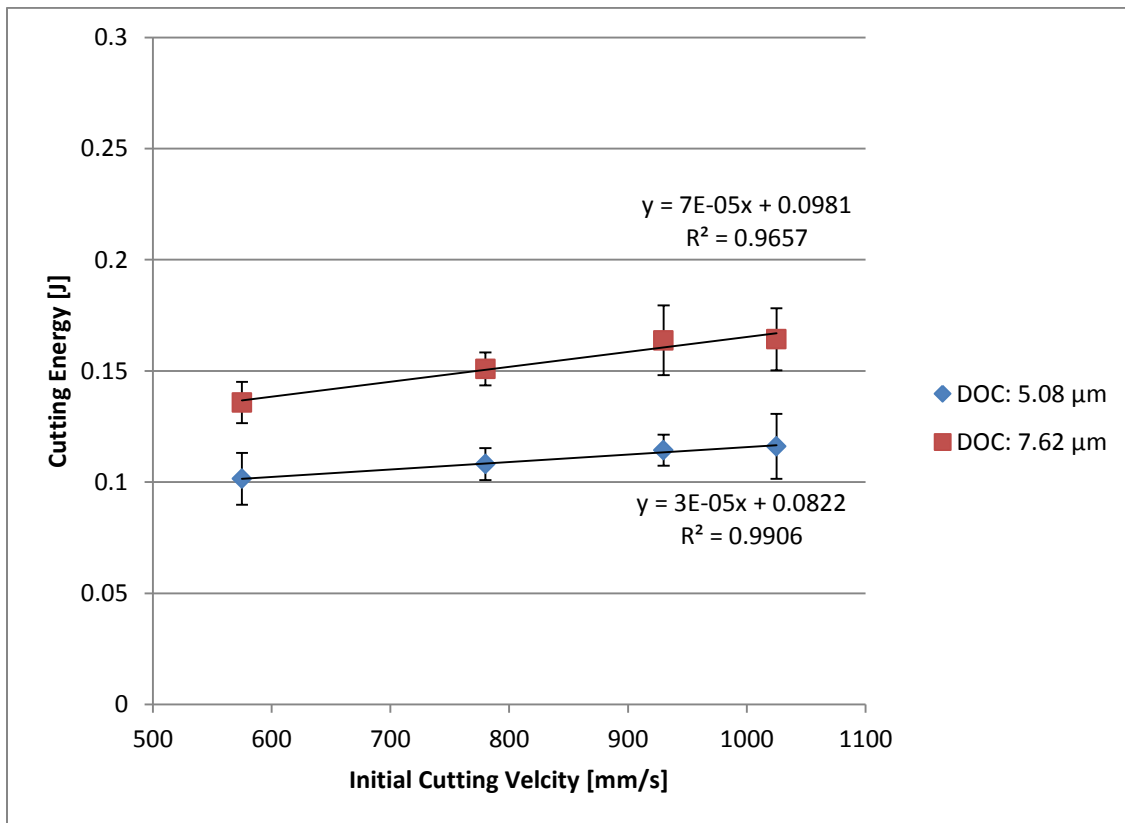
Figure 40: Effect of initial cutting velocity on cutting energy for a constant carriage mass (2014.5 g)

This screening experiment showed a slight linear cutting energy dependency on the initial cutting velocity, and therefore, is included as a factor in these experiments.

Depth of Cut Screening Experiments

The two previously-described screening experiments have hinted at the relationship between the cutting energy and depth of cut; however, a full screening experiment is still required. The cutting energy was measured at six separate depths of cut, all at one carriage mass (2014.5 g) and one initial cutting velocity (930 mm/s). The six depths of cut used in the experiment are shown in Table 7.

Table 7: Depths of Cut for depth of cut screening experiments

Depth of Cut [µm]	Depth of cut [in]
1.27	0.00005
2.54	0.0001
5.08	0.0002
7.62	0.0003
10.16	0.0004
12.70	0.0005

Three full replicates of these depth of cut screening experiments were completed in three different bone samples. With all other variables held constant, these results are shown in Figure 41.
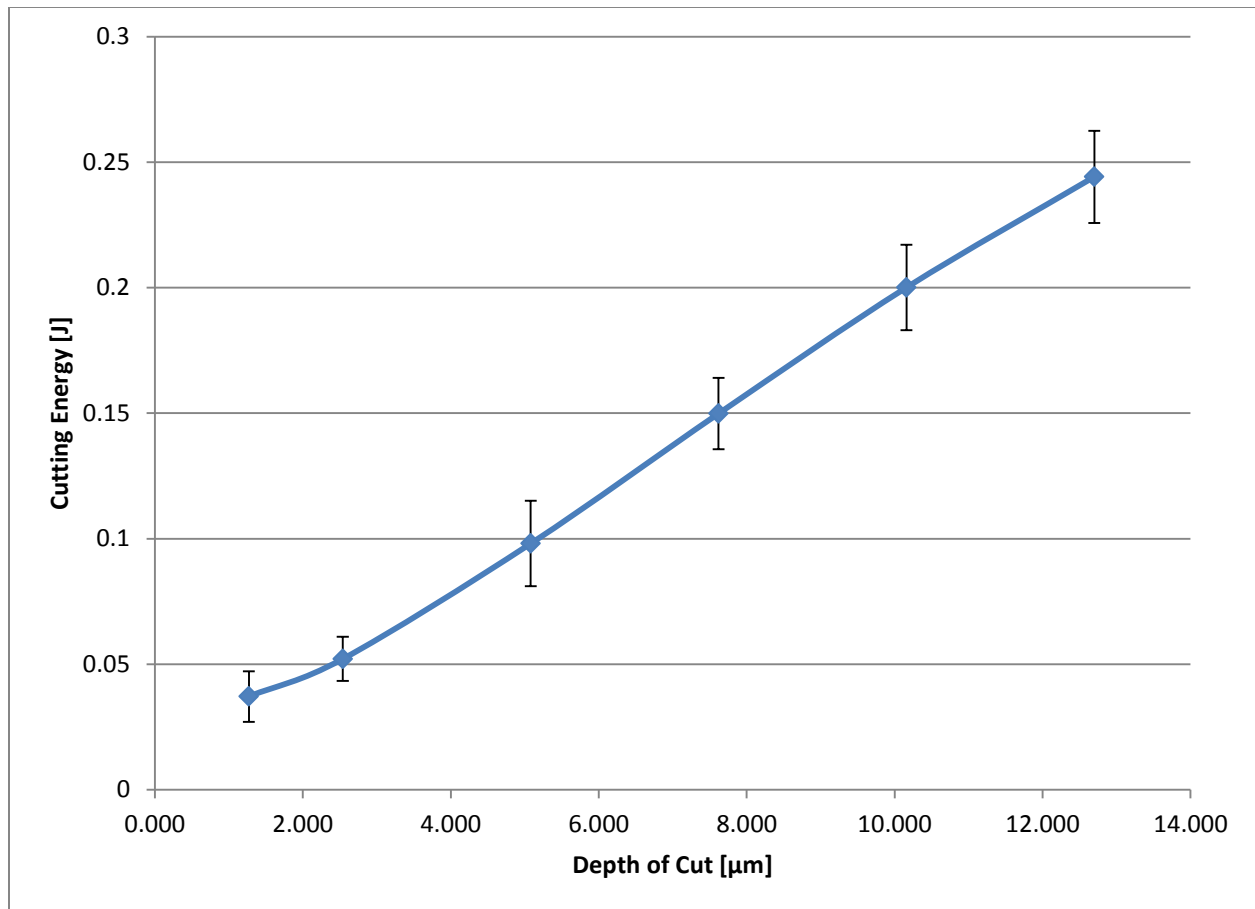
Figure 41: Depth of cut screening experiments summary
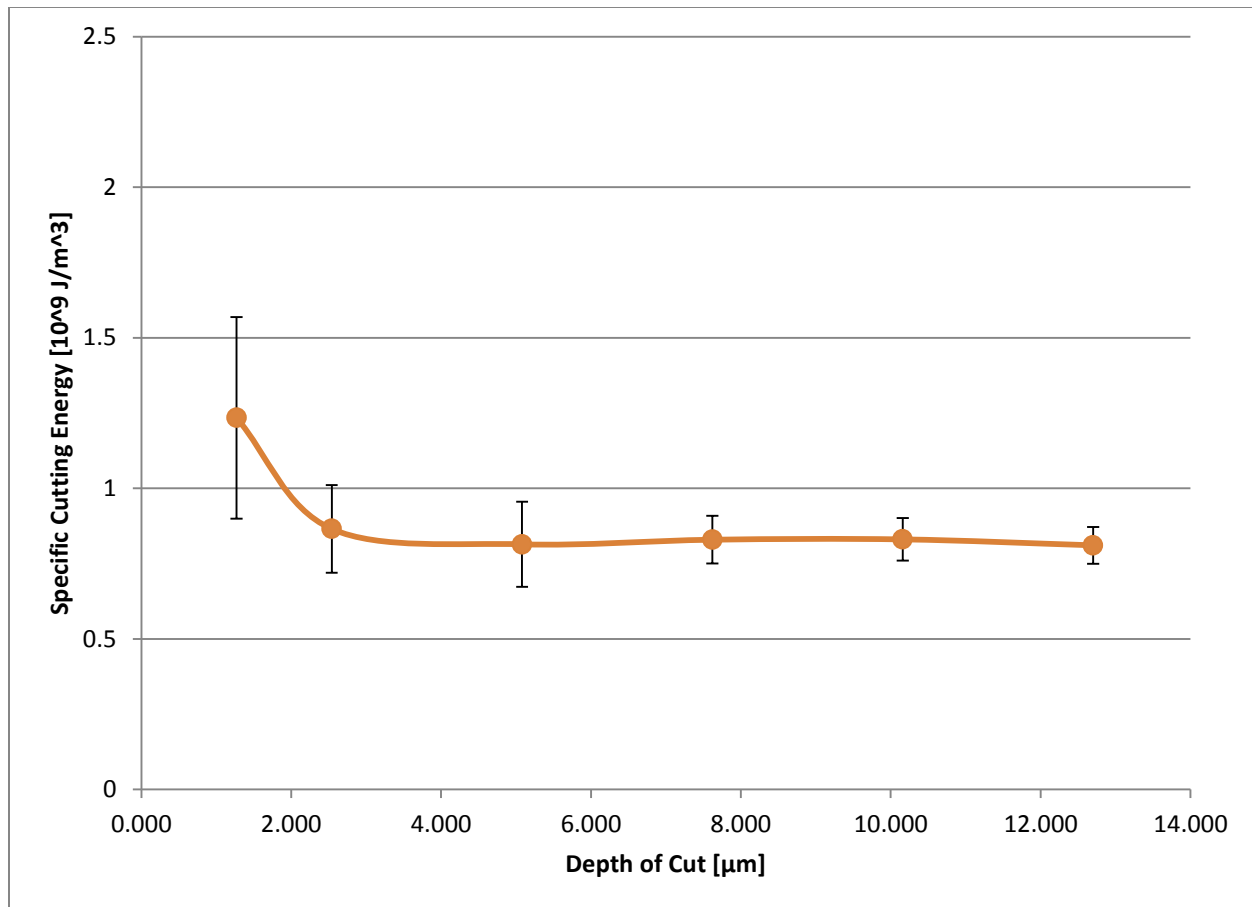
Figure 42: Average specific cutting energy for depth of cut screening experiments

The relationship between the depth of cut and cutting energy is shown to have a linear

dependence. It is also repeatable, as these three data sets are within one standard

deviation of each other.

Two-Factor, Two-Level Experiment

As the completed screening experiments have shown that carriage mass has no effect

on the cutting energy and the initial cutting energy and depth of cut have a linear

relationship with cutting energy, a two-factor, two-level design of experiments analysis

was chosen. The benefit of this type of factorial is that it represents the relationship

between factors with a linear response accurately [41].

It was decided to follow the depths of cut calculated by Lannin and Kelly to mimic real world cutting situations. These depths of cut chosen are also less than the radius of the Brasseler tooth, Figure 33, the area of interest. The levels of initial cutting velocity were chosen due to the linearity of the energy change between the values specified; values for both factors are shown in Table 8.

Table 8: Design of Experiment factors and values

Factors			
Depth of Cut [µm]		Initial Cutting Velocity [mm/s]	
10.16 (.0004")	2.54 (.0001")	930	575

The high level of the initial cutting velocity factor represents a 45% increase in initial kinetic energy relative to the low level of the factor. This span allows for the Design of Experiments factorial to represent a large range of initial cutting energies accurately.

With this two-factor, two-level experiment, there are four combinations of the experiment that can be completed; the numbering convention for these sets is described in Table 9.

Table 9: Experiment run numbering conventions

		D: Depth of Cut [µm]	
		2.54	10.16
A: Initial Cutting Velocity [mm/s]	575	4	3
	930	2	1

The full factorial experiment and related naming conventions are shown in Figure 43.
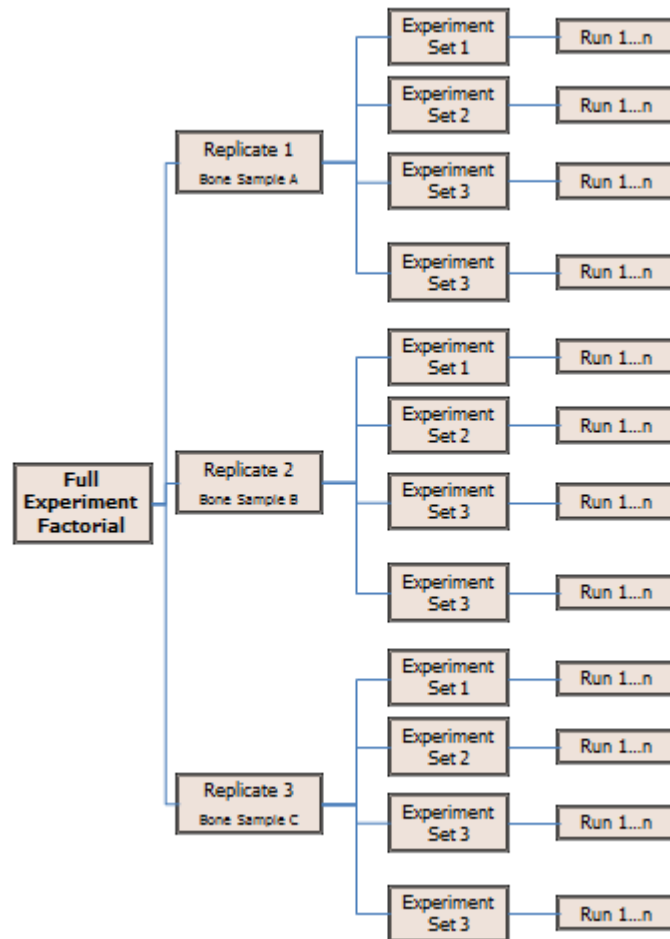
Figure 43: Naming conventions for experiments

Each replicate consisted of the same four experimental sets, the four combinations of factors described in Table 9. Each of these sets consisted of a minimum of 12 runs, allowing for a statistically significant conclusion about the energy change and forces in the cutting. These three replicates allowed for a conclusion to be reached that eliminated the variation between bone samples, as bone is known to be an extremely variable material.

Each bone sample was able to support the four experiment sets in four different locations on the sample, described in Figure 44.
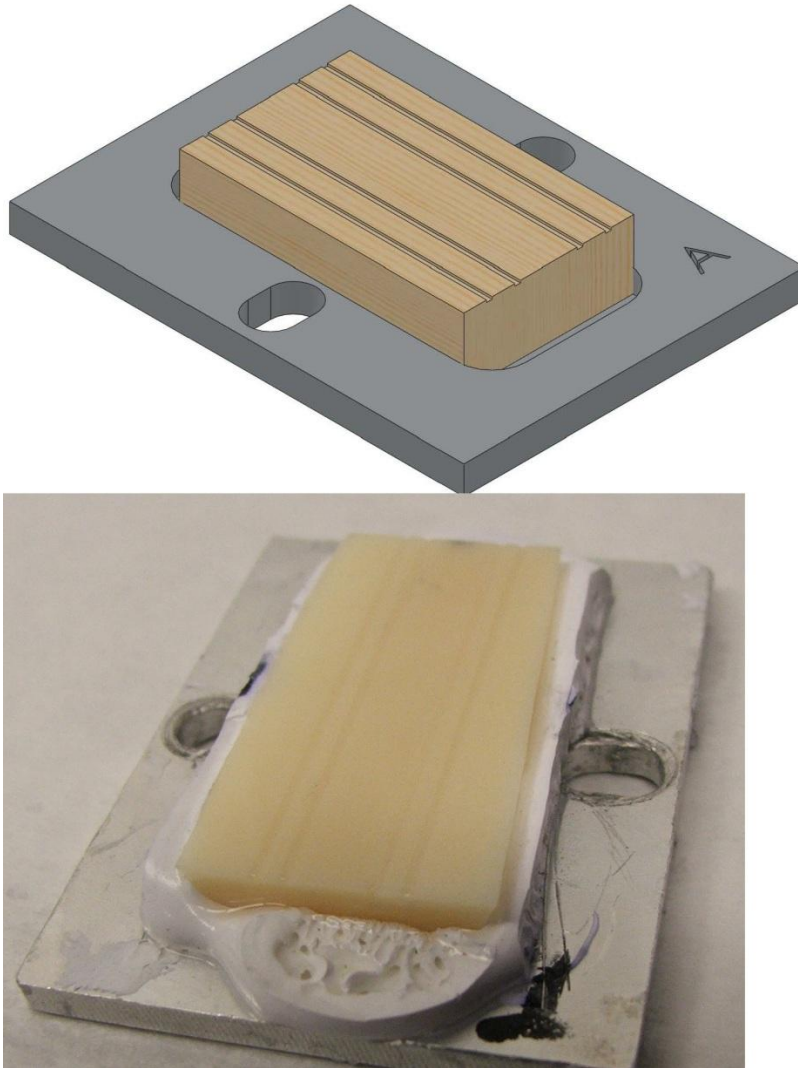
Figure 44: Images of four experimental run paths on bone samples

For each replicate of this experiment, the order of these four experimental sets was randomized to eliminate any location-bias impact on cutting event. The experimental procedure previously described was followed to complete the full experimental factorial.

Results

Upon completion of the full factorial and the data analysis, averages of ΔKE due to cutting, cutting force and thrust force were computed, as shown in Table 10, recall that the high and low factors for the initial cutting velocity were 575 mm/s and 930 mm/s. For the depth of cut, they were 10.16 μm and 2.54 μm (0.0004" and 0.0001"), respectively.

Table 10: Data averages for complete experimental factorial

Experimental Set	Initial Cut Vel. [mm/s]	DOC [μm]	ΔKE [J]	Cutting Force[N]	Thrust Force [N]	Ratio of Cutting force to Thrust force
1	930	10.16	0.148	4.082	5.178	0.788
2	930	2.54	0.063	1.736	3.107	0.559
3	575	10.16	0.153	4.306	5.290	0.814
4	575	2.54	0.060	1.697	2.720	0.624

These averages were taken from the following raw data figures.

8
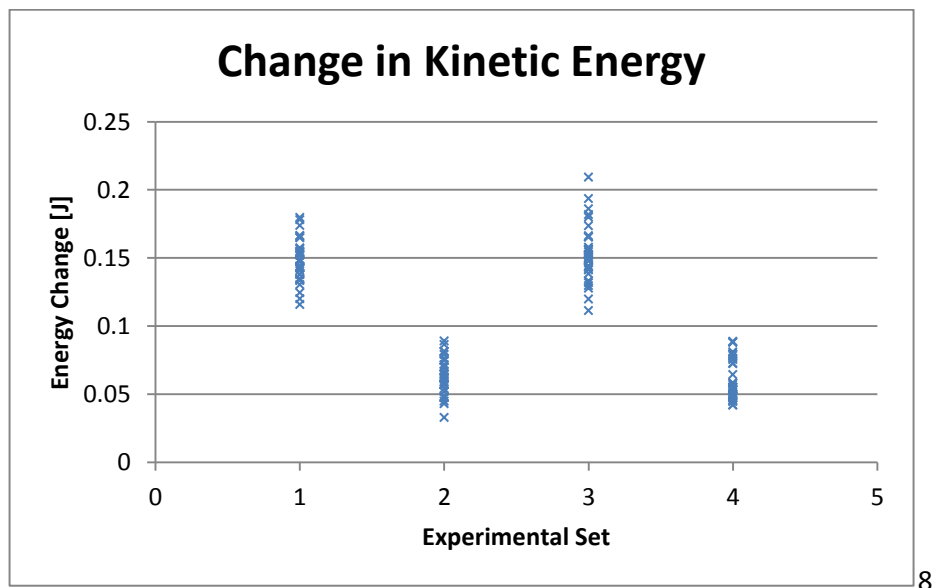
Figure 45: Kinetic energy change raw data
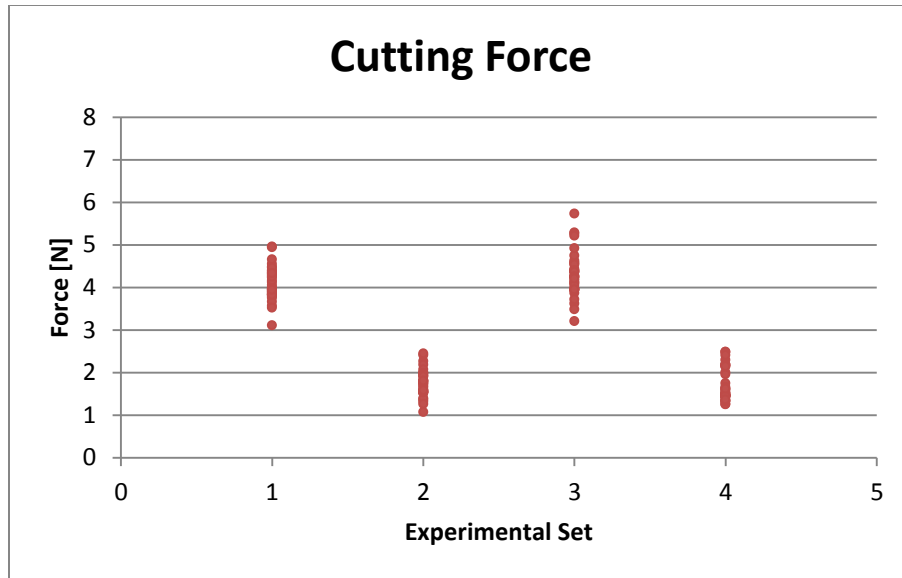
Figure 46: Cutting force raw data
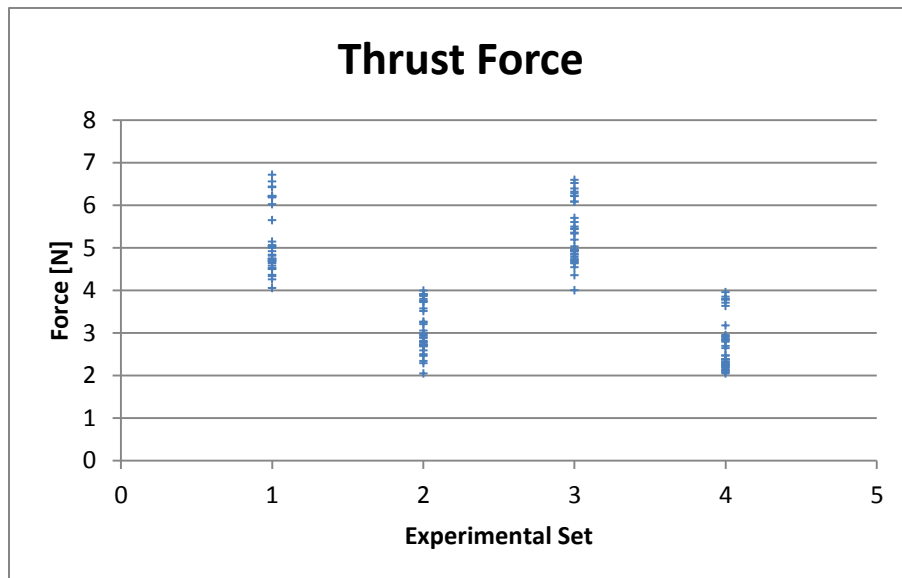
Figure 47: Thrust force raw data

The x-axis in these raw data plots corresponds to the experiment set number, which described the factor variables, as shown in Table 10.

The relationships between the factors and measured quantities were determined using a Design of Experiments approach, as shown in the following figures.
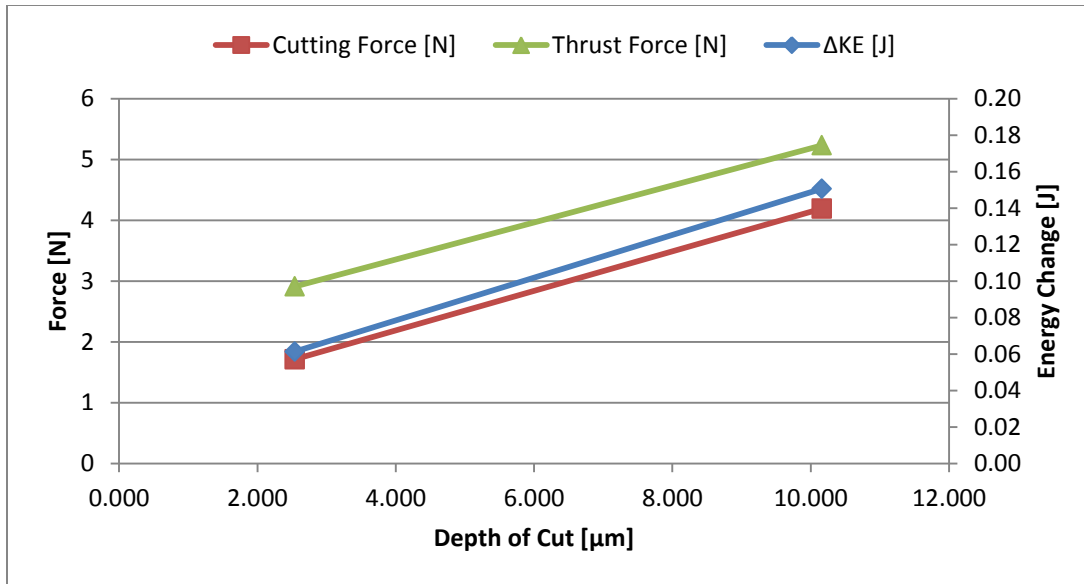
Figure 48: Effect of depth of cut on dependent variables
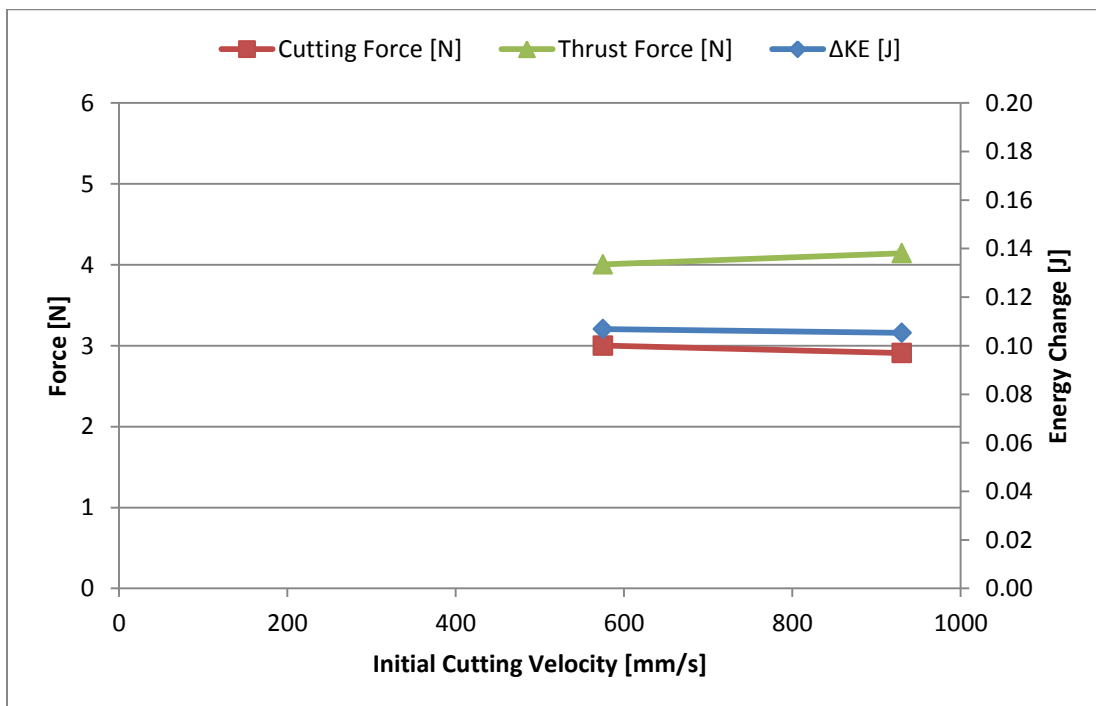
Figure 49: Effect of initial cutting velocity on dependent variables

The overall effect of the factors and their decision limits (DL) are shown in Figure 50, below. The decision limits were determined using standard Design of Experiment equations, and a confidence level of 95%.
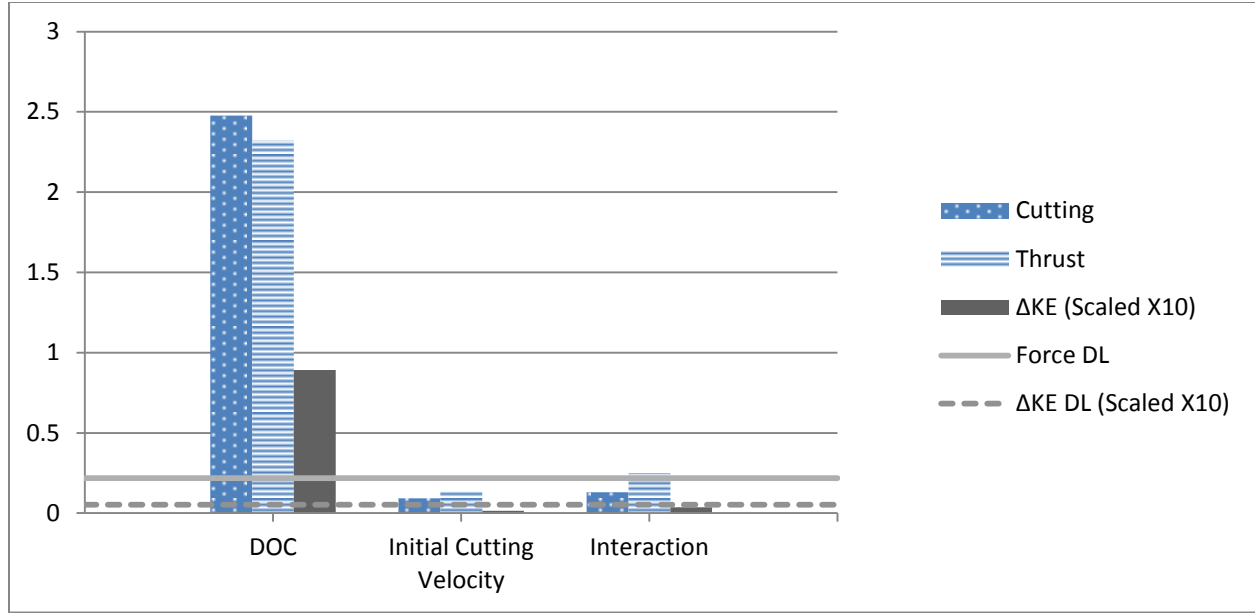
Figure 50: Effects and decision limits of experimental factors

The main point to take from Figure 50 is that the only factor that has an effect on either of the measured quantities, force or cutting energy, is the depth of cut.

The Design of Experiments technique allows for the derivation of equations that model the effect of the factors on the dependent variables. These equations are shown below;

$$\Delta KE = .106 + (0.04465) * DOC_{Scaled}$$

$$F_C = 2.955 + (1.239) * DOC_{Scaled}$$

$$F_T = 4.073 + (1.16) * DOC_{Scaled}$$

Where the scaled depth of cut is calculated using the depth of cut in μm by the equation;

$$DOC_{Scaled} = 0.2625 * (DOC) - 1.667 \qquad (12)$$

Resulting in the following equations for predicting the dependent variables;

$$\Delta KE = 0.0316 + 0.0117 * DOC \qquad (13)$$

$$F_C = 0.89 + 0.325 * DOC \qquad \text{(14)}$$

$$F_T = 2.139 + 0.3045 * DOC \qquad \text{(15)}$$

To verify the accuracy of these equations, a sample calculation was completed to verify

that the kinetic energy change calculated matched the screening experiments. This

calculation was completed for a depth of cut of 5.08 μm.

$$\Delta KE = 0.0316 + 0.0117 * DOC$$

$$\Delta KE = 0.0316 + 0.0117 * (5.08) = 0.091\,J$$

In comparing this to the measured energy change during the previously described

screening experiments it is shown to be within one standard deviation, 0.017 J, of the

average value, 0.098 J, at this depth of cut, shown in Figure 41.

Discussion

When examining the force diagram at the tool/bone interface, it can be seen that the two measured forces, cutting and thrust, can be combined into a resultant force, as shown in Figure 51.
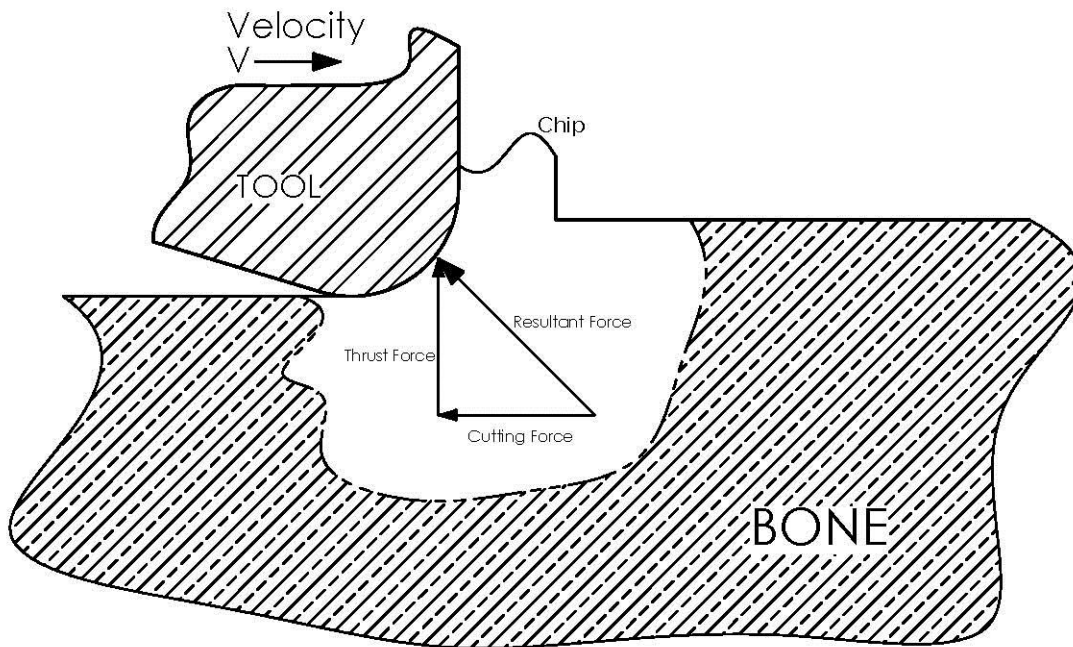
Figure 51: Overall force diagram at tool/bone interface

As the measured change in velocity from the encoder represents an overall change in kinetic energy, it can be concluded that this is the overall work due to the resultant force. Therefore, to quantify the amount of elastic deformation during cutting of bone, the measured change in kinetic energy was compared to the work due to the force in the cutting direction, by means of the work-energy theorem. To calculate the amount of work done by this cutting force, Equation (**16**) was utilized.

$$W = Fd \qquad\qquad (16)$$

Upon a quick examination, one would assume that the work of elastic deformation of the bone could easily be calculated, as both cutting and thrust forces were measured in

74

these experiments. However, the distance that the thrust force acts over is uncertain in this case; just how much bone actually deflects underneath the tool is unknown. Conversely, the cutting distance related to the cutting force is known with great accuracy, as the bone sample is measured using a Mitutoyo digital caliper. Using this measurement and Equation (**16**), the work of this cutting force then is determined. As previously described, the energy determined from the position encoder, ΔKE, was the energy expended over the entire cutting event resulting from both the cutting and thrust forces. Therefore, when the energy expenditure due to the cutting force is subtracted from this overall energy change, the resultant is the energy expenditure associated with the thrust force.

$$\Delta KE - W_{Fc} = W_{Ft}$$

$$\Delta KE - (F_C l) = W_{Ft} \qquad (17)$$

In Table 11, the values of Table 10 have been reiterated with the addition of the work due to the cutting force along with this new calculated value of so-called thrust force work, or elastic energy.

Table 11: Data averages for full factorial experiment, including work due to thrust force

Exp. Set	Initial Cut Vel. [mm/s]	DOC [µm]	ΔKE [J]	Cutting Force, F_C [N]	Thrust Force, F_T [N]	Work in Cutting Direction, W_{FC} [J]	Work in Thrust Direction, W_{FT} [J]
1	930	10.16	0.148	4.082	5.178	0.153	-0.005
2	930	2.54	0.063	1.736	3.107	0.065	-0.002
3	575	10.16	0.153	4.306	5.290	0.161	-0.008
4	575	2.54	0.060	1.697	2.720	0.064	-0.004

The value of this elastic energy is of such a small magnitude that it can be attributed to any uncertainty in the measurement. See appendix for the uncertainty analysis.

Therefore, during these cutting events, the energy absorbed can be accounted for completely by the work due to the force in the cutting direction. It is also important to note that during all experiments, including the screening experiments for all factors, bone debris was observed even at the lowest depth of cut in these experiments. This is a qualitative confirmation that the elastic deformation is small, if existent, compared to the plastic deformation of the bone.

In relating this calculation to the physical model of cutting at small depths of cut, the research of Jun et al and Waldorf is of interest. Waldorf details his separation-point model in which a point is described on the tool tip radius, above which the work-material flows upward into the chip, and below which the material is compressed into the work piece [28]. The cutting force model developed by Jun utilizes this separation point to calculate the cutting forces in his model, which includes a component of force due to the material being forced underneath the tool [31]. Figure 52 shows a physical representation at the tool tip of the material being forced in both directions.
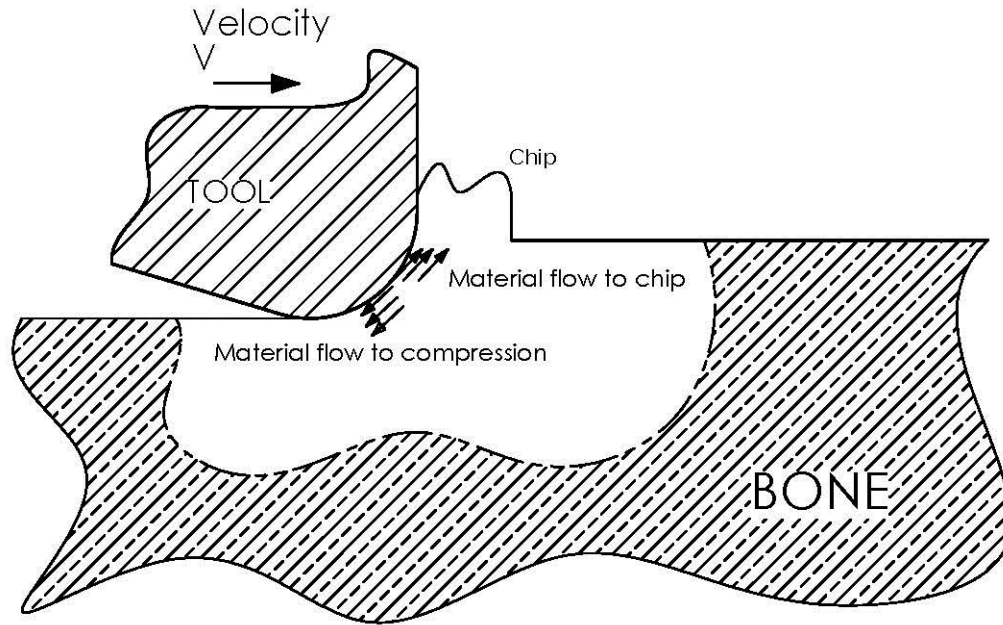
Figure 52: Description of material flow from separation point

Using the reasoning from both Jun and Waldorf, it would seem that as material flows underneath the tool, there would be work done by the thrust force that was not accounted for in the work due to the cutting force. Yet in the experiments of this thesis on bone, there was no measurable work done by the thrust force.

A basic theoretical calculation was completed to answer the question of whether or not the work due to the thrust force would be measureable. Using a tool tip radius of .013 mm (.0005") and the smallest depth of cut, 2.54 µm (0.0001"), the number of incremental locations of the tool along the length of the sample was calculated. At each incremental position, the thrust force would vertically compress the work piece a distance of the depth of cut, see Figure 53. This allowed for the calculation of the total vertical distance that the thrust force was acting on, based on the number of

incremental positions, which is used to calculate theoretical thrust work, as shown in

Figure 54.
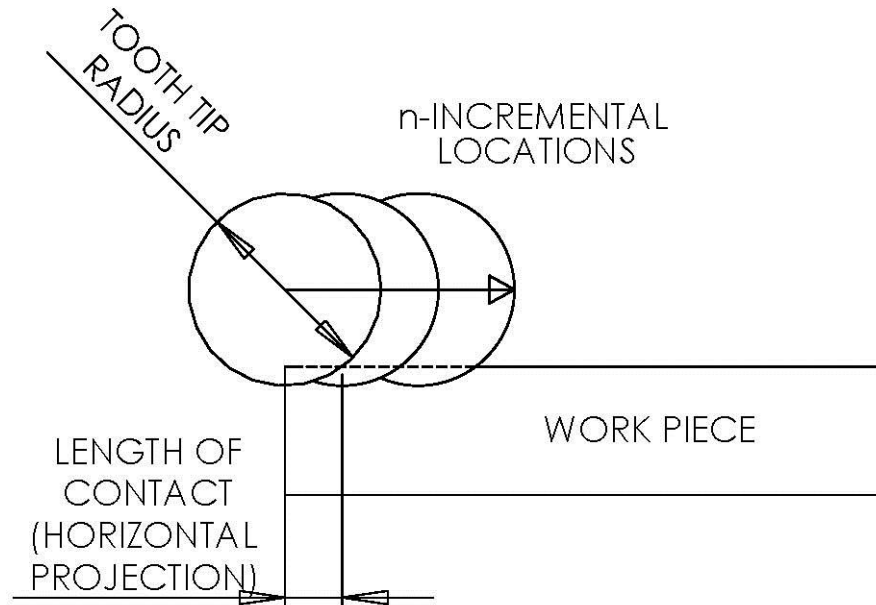
Figure 53: Diagram showing n-incremental locations as tool traverses the work piece. At each incremental location the thrust force theoretically displaces the bone by the depth of cut.

HORIZONTAL PROJECTION = .0076 MM
SAMPLE LENGTH = 37.465 MM

THERE ARE THEN :

$$\frac{37.465}{.0076} = 4930 \text{ INCREMENTAL TOOL SECTIONS}$$

WHERE THE BONE IS PUSHED

UNDERNEATH THE TOOL

TOTAL VERTICAL DISTANCE:
d = 4930*.0025 = 12.325 MM

AVERAGE THRUST FORCE = 3 N
THEORETICAL THRUST WORK:
$$W_T = 3*\frac{12.325}{1000} = 0.037 \text{ J}$$
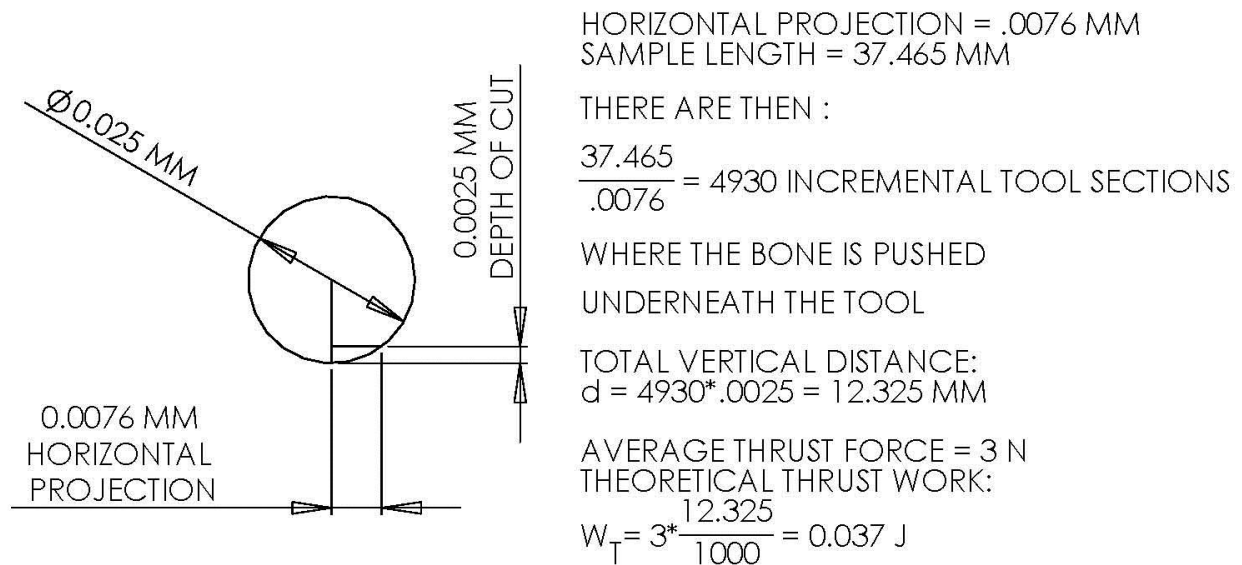
Figure 54: Calculation of upper-bound theoretical work due to thrust force

This calculated upper-bound theoretical thrust work, 0.037 J, is certainly of a

measurable magnitude, as during the screening experiments, energy changes smaller

than this were measured consistently. As this thrust force work would be of a

measurable magnitude, it then follows that negligible work was done by the thrust

force.

Coupled with the observance of bone debris at all experimental depths of cut, the result

that no measurable work was done by the thrust force implies that negligible bone flows

underneath the tool during the cutting event. The result is a material flow that is

depicted in Figure 55, below.
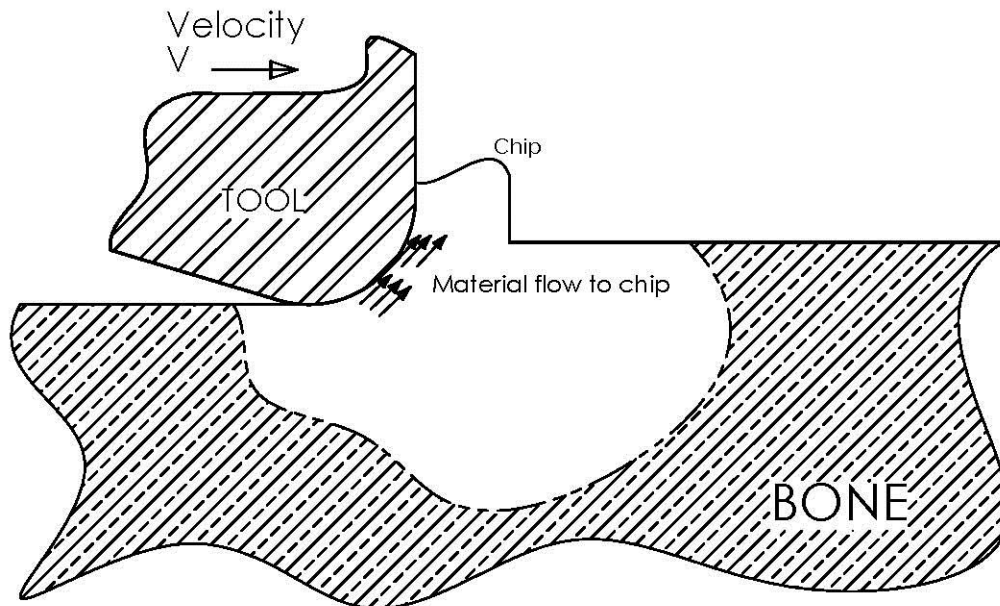
Figure 55: Theorized material flow, note none flows under the tool

Images from a 2009 Sugita and Mitsuishi article about machining bovine cortical bone

are of interest to this thesis. Published images show chip formation during cutting

parallel to the bone osteons at a depth of cut of 10 μm (.0004"), Figure 1b in the

published article [42]. The image of interest shows that at this depth of cut, there is

clearly a continuous chip developed, and the uncut chip thickness (depth of cut) is the

same as the cut chip thickness. Despite the diamond tool used, the tool tip radius is of a

similar order of magnitude as the depth of cut, and in their cutting experiments, no

material was seen to flow underneath the tool. Their research is a visual confirmation of

the results obtained in this thesis by measuring the cutting energy and comparing it to

the work of cutting. The determined negligible work due to the thrust force implies that

all of the energy goes into friction and fracture to generate a chip.

Conclusions

Using an experimental fixture that captured position data of a falling carriage, the energy of cutting bovine bone was quantified while, concurrently, cutting and thrust forces of these cutting events were recorded using a dynamometer. During these cutting experiments, it was observed that at all depths of cut tested, from 1.27 μm to 12.70 μm (0.00005" to 0.0005"), bone debris or chips were formed. Upon comparison of the energy calculated from the tool carriage position data and the work done by the measured forces, the conclusion was reached that the thrust force does negligible work on the bone during the cutting event. In the absence of work from the thrust force, an appropriate material flow model, for these depths of cut, necessitates that all of the material flow into the chip creation. It does not appear that bone is pushed underneath the tool. It is this conclusion and material flow model that relates to the hypothesis of this thesis, reiterated here: **elastic deformation during the cutting of bone, which does not contribute to chip formation, is a significant contributor to the energy required to cut.**

As it has been shown that the energy of cutting is fully accounted for in the cutting work, there is negligible elastic deformation in the described cutting experiments. Therefore, the initial hypothesis for this thesis has been proven false. There is essentially no elastic deformation at depths of cut common to bone sawing. Material flowing underneath the tool does not contribute significantly to the energy required to cut.

The experiments of this thesis have shown that the only experimental factor to have a

significant effect on both the energy change and the forces is the depth of cut. The

initial cutting velocity of the tool carriage does not have an effect on the cutting forces

and energy of cutting. The relationship between the depth of cut and cutting energy is

linear within the range that was investigated.

Recommendations for Future Research

There are many paths that future researchers could take utilizing this newly designed apparatus. Direct continuation of the current research should include the use of a higher resolution micrometer, so the depth of cut could be controlled to an accuracy of .254 μm (.00001"). This may facilitate the measurement of the exact amount of elastic energy in this cutting event. In addition, taking high speed video of the cutting event, at any depth of cut, could lead to interesting conclusions for the mechanism of chip formation. Finally, this fixture could be used to quantify cutting energy for different blade geometries.

The broader impact of this research is on bone cutting during surgery. It would be wise to replace the bovine bone with human bone. This would allow for replication and assurance that the conclusions from this thesis could be extended to human bone. In addition, as thermal effects are of concern, it would be useful to model and measure the thermal changes of the bone during the cutting event.

Works Cited

[1] Smith & Nephew Inc., "ConquestFX Tapered Hip System Surgical Technique," 1999.

[2] Brasseler USA. (2011) Brasseler Catalog. [Online]. http://www.brasselerusamedical.com/Brasseler_USA_Catalog_8.pdf

[3] R. Wachter and P. Stoll, "Increase of temperature during osteotomy," *International Journal of Oral Maxillofacial Surgery*, pp. 245-249, 1991.

[4] Akron General Hospital. (2010, Jan) Akron General. [Online]. http://www.akrongeneral.org/portal/page/portal/AGMC_PAGEGROUP/Price_guide/PRICE_GUIDE5

[5] Albrektsson Eriksson, "Temperature threshold levels for heat-induced bone tissue injury: A vital-microscopic study in the rabbit," *Journal of Prosthetic Dentistry*, pp. 101-107, 1983.

[6] Albrektsson Eriksson, "Thermal Injury to Bone A Vital-microsopic description of heat effects," *International Journal of Oral Surgery*, pp. 115-121, 1982.

[7] K. Alam and A. Mitrofanov, "Temperature Calculations in Orthogonal Cutting of Cortical Bone Using Finite Element Analysis," in *25th Southern Biomedical Engineering Conference*, 2009, pp. 151-152.

[8] Stryker Instruments, "Sagittal and Reciprocating Saw Blades Poster," 2006.

[9] Timothy Lannin, "Cutting Rate Performance of a Novel Reciprocating Bone Saw," Tufts University, Medford, MA, Undergraduate Research Thesis 2011.

[10] Matthew P. Kelly, "Novel Sagittal Bone Saw," Tufts University, Medford, MA, Undergraduate Research Thesis 2011.

[11] S. Malak and I. Anderson, "Orthogonal cutting of cancellous bone with application to the harvesting of bone autograft," *Medical Engineering and Physics*, vol. 30, pp. 717-724, 2008.

[12] K.L. Wiggins and S. Malkin, "Orthogonal Machining of Bone," *Journal of Biomechanical Engineering*, vol. 100, pp. 122-130, August 1978.

[13] M. E. Merchant, "Mechanics of the metal cutting process, I: orthogonal cutting," *Journal of Applied Physics*, pp. 267-275, 1945.

[14] M. Bäker, "Does chip formation minimize the energy?," *Computational Materials Science*, vol. 33, pp. 407-418, 2005.

[15] Molinari and Moufki, "The Merchant's model of orthogonal cutting revisited: A new insight into the modeling of chip formation," *International Journal of Mechanical Sciences*, pp. 124-131, 2008.

[16] Thomas James, *Application of Cutting Mechanics to Reciprocating Sawing; PhD Dissertation*. Milwaukee: Marquette University, 2002.

[17] Gerard Tortora and Sandra Reynolds Grabowski, *Introduction to the Human Body: Essentials of Anatomy and Phisiology*. Hoboken NJ: John Wiley & Sons, 2004.

[18] John D. Currey, *Bones: Structure and Mechanics*. Princeton, NJ: Princeton University Press, 2002.

[19] A.N. Natali and E.A. Meroi, "A review of the biomechanical properties of bone as a material," *Journal of Biomedical Engineering*, vol. 11, pp. 266-276, July 1989.

[20] I Knets and A Melnis, "Effect of Time Dependence on the Mechanical Behavior of Compact Bone Tissue," in *IUTAM Symposium on Synthesis in Bio Solid Mechanics*, Netherlands, 1999, pp. 129-138.

[21] Jae-Young Rho and Liisa Kuhn-Spearing, "Mechanical properties and the hierarchical structure of bone," *Medical Engineering and Physics*, vol. 20, pp. 92-102, December 1998.

[22] I. Sevostianov and M. Kachanov, "Impact of the porous microstructure on the overall elastic

properties of the osteonal cortical bone," *Journal of Biomechanics*, vol. 33, pp. 881-888, 2000.

[23] P. Zysset and X. Guo et. al., "Elastic modulus and hardness of cortical and trabecular bone lamellae measured by nanoindentation in the human femur," *Journal of Biomechanics*, vol. 32, pp. 1005-1012, 1999.

[24] S. Malak and I. Anderson, "Orthogonal cutting of polyurethane foam," *International Journal of Mechanical Sciences*, vol. 47, pp. 867-883, 2005.

[25] William Robert Krause, *Mechanical Effects of Orthogonal Bone Cutting, PhD Dissertation*. Clemson: Clemson University, 1976.

[26] M.J. Jackson and G.M. Robinson et. al., "Machining Cancellous Bone Prior to Prosthetic Implantation," *Journal of Materials Engineering and Performance*, vol. 14, no. 3, pp. 293-300, June 2005.

[27] P. Albrecht, "New Developments in the Theory of the Metal-Cutting Process: Part I. The Ploughing Process in Metal Cutting," *Journal of Engineering for Industry/Transactions of the ASME*, pp. 348-358, November 1960.

[28] D.J. Waldorf and R.E. DeVor, "An Evaluation of Ploughing Models for Orthogonal Machining," *Journal of Manufacturing Science and Engineering/Transactions of the ASME*, vol. 121, pp. 550-558, November 1999.

[29] P.K. Basuray, B.K. Misra, and G.K. Lal, "Transition from Ploughing to Cutting During Machining with Blunt Tools," *Wear*, vol. 43, pp. 341-349, 1977.

[30] M. Es. Abdel Moneim, "Comments on "Transition from ploughing to cutting during machining with blunt tools"," *Wear*, vol. 64, no. 2, pp. 385-387, November 1980.

[31] Martin Jun, Chanseo Goo, Mohammad Malekian, and Simon Park, "A New Mechanistic Approach for Micro End Milling Force Modeling," in *Proceedings of the ASME 2010 International Mechanical Engineering Congress & Exposition*, Vancouver, BC, 2010.

[32] Thomson Linear, *Profile Rail Linear Guides 500 Series*.: Thomson Linear Motion, 2004.

[33] Renishaw, "MS magnetic scale installation guide LM10D02_06," 2010.

[34] Renishaw, "LM10 linear magnetic encoder system installation LM10D06_06,".

[35] Kistler Instrument Corporation. 75 John Glenn Drive; Amherst, NY 14428.

[36] Blood-Farm. 94 West Main Street; Groton MA 01472.

[37] invitrogen, Life technologies. (2011) Technical Resources Hanks' Balanced Salt Solution. [Online]. http://www.invitrogen.com/site/us/en/home/support/Product-Technical-Resources/media_formulation.154.html

[38] 3M, "3M Marine Adhesive Fast Cure 5200 Data Sheet," Saint Paul, MN, 2006.

[39] Brasseler USA Medical LLC, *Brasseler USA Product Catalog*. Savannah, Georgia, 2006, vol. 8.

[40] Larry Barrentine, *An Introduction to Design of Experiments*. Milwaukee, WI: ASQ Quality Press, 1999.

[41] Charles Hicks and Kenneth Turner Jr. , *Fundamental concepts in the Design of Experiments*, 5th ed. New York, NY: Oxford University Press, 1999.

[42] Naohiko Sugita and Mamoru Mitsuishi, "Specifications for machining the bovine cortical bone in relation to its microstructure," *Journal of Biomechanics*, vol. 42, pp. 2826-2829, 2009.

Appendix

Energy Uncertainty

Renishaw data from LM10 data sheet

Resolution: 10 µm

Error: ±3.5 µm (below 0.7 mm ride height)

$$U_E = \sqrt{(3.5\mu m)^2 + \left(\frac{10\mu m}{w}\right)^2} = \pm 6.1\mu m$$

Mass uncertainty:

Resolution of balance: 0.1 g

Use these uncertainties in the equation for energy

$$E = \frac{1}{2}mV^2$$

$$E = \frac{1}{2}(0.0001KG)\left(\frac{2*6.1\mu m}{0.001s}\right) = 0.61\mu J$$

$$U_E = \pm 0.61\mu J$$

Force Uncertainty

Kistler Dynamometer 9047c:

Sensitivity: $36.25 \frac{pC}{lbf}$

Kistler Charge Amplifier 5004:

Sensitivity: $1 \pm 0.5\% \frac{pC}{mV}$

Accuracy: ±1 %

Therefore the Sensitivity of the Dynamometer/charge amp connection is:

$$\frac{36.25 \frac{pC}{lbf}}{1 \frac{pC}{mV}} = 36.25 \frac{mV}{lbf} = 0.03625 \frac{V}{lbf}$$

So, the 1.5% accuracy is at this sensitivity:

$$.015 * .03625 \frac{V}{lbf} = .00054 \frac{V}{lbf}$$

As the charge amplifier scale used was 1 V = 1 lbf;

The overall force uncertainty is:

$$U_F = \pm 0.00054 \; lbf = \; \pm 0.0024 \; N$$

Sample Work of Thrust Calculation

Factors:

Depth of Cut:	0.0102 mm
Initial Cutting Velocity:	930 mm/s

Measured kinetic energy change: 0.149 J

Measured cutting force: 3.964 N

Length of work-piece (bone):   37.944 mm

Calculated work of cutting force: $W_C = F_C * d = (3.964 \; N) * (37.944 \; mm) =$

$0.150J$

Calculated work of thrust force: $W_T = \Delta KE - W_C = (0.149 \; J) - (0.150 \; J) =$

$-0.001 \; J$

Raw Experimental Data

Run	Depth of Cut: 0.0102 mm			Initial Cut Velocity: 930 mm/s							
	Energy Change [J]	Cutting Force [Lbs]	Cutting Force [N]	Energy of Cutting Force [J]	Work of Thrust [J]	Thrust Force [lb]	Thrust Force [N]	Ratio Thrust/Cutting	Ratio Cutting/Thrust		MM
1	0.116	0.699	3.109	0.118	-0.002	0.911	4.054	1.304	0.767	Sample Length (1-12)	37.944
2	0.135	0.801	3.564	0.135	-0.001	1.018	4.530	1.271	0.787		
3	0.147	0.885	3.937	0.149	-0.002	1.087	4.836	1.228	0.814		
4	0.157	0.899	4.001	0.152	0.005	1.106	4.918	1.229	0.813		
5	0.147	0.844	3.755	0.142	0.005	1.081	4.811	1.281	0.781		
6	0.143	0.951	4.230	0.160	-0.017	1.156	5.142	1.216	0.823		
7	0.152	0.912	4.056	0.154	-0.002	1.128	5.018	1.237	0.808		
8	0.180	1.114	4.956	0.188	-0.008	1.056	4.696	0.948	1.055		
9	0.147	0.858	3.817	0.145	0.002	0.980	4.361	1.143	0.875		
10	0.149	0.891	3.964	0.150	-0.002	1.011	4.496	1.134	0.882		
11	0.153	0.926	4.120	0.156	-0.003	1.030	4.580	1.112	0.900		
12	0.144	0.863	3.839	0.146	-0.002	1.014	4.511	1.175	0.851		
13	0.130	0.850	3.783	0.142	-0.012	1.126	5.010	1.324	0.755		MM
14	0.135	0.892	3.966	0.149	-0.014	1.270	5.648	1.424	0.702	Sample Length (13-24)	37.613
15	0.144	0.935	4.159	0.156	-0.013	1.354	6.022	1.448	0.691		
16	0.148	0.984	4.375	0.165	-0.016	1.390	6.181	1.413	0.708		
17	0.153	0.968	4.305	0.162	-0.009	1.396	6.211	1.443	0.693		
18	0.157	0.961	4.277	0.161	-0.004	1.394	6.202	1.450	0.690		
19	0.166	1.007	4.478	0.168	-0.002	1.443	6.419	1.433	0.698		
20	0.166	1.023	4.550	0.171	-0.005	1.448	6.439	1.415	0.707		
21	0.174	1.046	4.652	0.175	-0.001	1.474	6.556	1.409	0.710		
22	0.165	0.988	4.396	0.165	0.000	1.398	6.220	1.415	0.707		
23	0.178	1.111	4.944	0.186	-0.008	1.510	6.716	1.358	0.736		
24	0.165	0.977	4.345	0.163	0.001	1.397	6.212	1.430	0.699		
25	0.120	0.824	3.666	0.135	-0.015	0.974	4.330	1.181	0.847		
26	0.125	0.792	3.523	0.130	-0.005	0.956	4.254	1.208	0.828		MM
27	0.143	0.877	3.901	0.144	-0.001	1.044	4.642	1.190	0.840	Sample Length (25-36)	36.848
28	0.138	0.879	3.910	0.144	-0.006	1.052	4.678	1.197	0.836		
29	0.134	0.862	3.836	0.141	-0.008	1.056	4.698	1.225	0.817		
30	0.143	0.869	3.865	0.142	0.000	1.065	4.740	1.226	0.815		
31	0.138	0.872	3.877	0.143	-0.005	1.067	4.744	1.224	0.817		
32	0.133	0.859	3.822	0.141	-0.007	1.064	4.734	1.239	0.807		
33	0.155	0.955	4.250	0.157	-0.001	1.137	5.059	1.190	0.840		
34	0.154	1.003	4.460	0.164	-0.010	1.135	5.049	1.132	0.883		
35	0.141	0.887	3.944	0.145	-0.005	1.049	4.668	1.184	0.845		
36	0.154	0.973	4.328	0.159	-0.005	1.125	5.003	1.156	0.865		
Avg.	0.148	0.918	4.082	0.153	-0.005	1.164	5.178	1.266	0.797		

Run	Depth of Cut: 0.0025 mm			Initial Cut Velocity: 930 mm/s							
	Energy Change [J]	Cutting Force [Lbs]	Cutting Force [N]	Energy of Cutting Force [J]	Work of Thrust [J]	Thrust Force [lb]	Thrust Force [N]	Ratio Thrust/Cutting	Ratio Cutting/Thrust		MM
1	0.087	0.509	2.262	0.086	0.001	0.720	3.202	1.415	0.706	Sample Length (1-12)	37.944
2	0.082	0.491	2.182	0.083	-0.001	0.731	3.252	1.490	0.671		
3	0.058	0.347	1.545	0.059	-0.001	0.582	2.590	1.676	0.597		
4	0.057	0.346	1.540	0.058	-0.001	0.604	2.685	1.743	0.574		
5	0.062	0.387	1.722	0.065	-0.003	0.659	2.930	1.702	0.588		
6	0.057	0.340	1.511	0.057	0.000	0.613	2.725	1.803	0.555		
7	0.057	0.370	1.648	0.063	-0.005	0.651	2.897	1.759	0.569		
8	0.057	0.343	1.525	0.058	-0.001	0.611	2.716	1.781	0.562		
9	0.062	0.357	1.587	0.060	0.002	0.631	2.809	1.770	0.565		
10	0.052	0.306	1.361	0.052	0.000	0.561	2.494	1.832	0.546		
11	0.070	0.394	1.753	0.067	0.003	0.665	2.959	1.688	0.592		
12	0.057	0.346	1.538	0.058	-0.002	0.604	2.685	1.746	0.573		
13	0.089	0.540	2.403	0.090	-0.001	0.879	3.911	1.628	0.614		MM
14	0.076	0.450	2.003	0.075	0.001	0.853	3.796	1.895	0.528	Sample Length (13-24)	37.613
15	0.075	0.465	2.067	0.078	-0.003	0.898	3.996	1.933	0.517		
16	0.079	0.446	1.983	0.075	0.005	0.876	3.896	1.965	0.509		
17	0.067	0.442	1.967	0.074	-0.007	0.869	3.864	1.964	0.509		
18	0.070	0.393	1.750	0.066	0.004	0.803	3.572	2.042	0.490		
19	0.075	0.405	1.801	0.068	0.007	0.844	3.755	2.085	0.480		
20	0.062	0.379	1.684	0.063	-0.001	0.790	3.514	2.087	0.479		
21	0.070	0.431	1.916	0.072	-0.002	0.876	3.897	2.034	0.492		
22	0.061	0.408	1.814	0.068	-0.007	0.841	3.743	2.064	0.485		
23	0.065	0.403	1.793	0.067	-0.002	0.837	3.725	2.078	0.481		
24	0.072	0.434	1.931	0.073	-0.001	0.878	3.907	2.023	0.494		
25	0.081	0.549	2.440	0.090	-0.009	0.733	3.261	1.336	0.748		
26	0.063	0.428	1.905	0.070	-0.007	0.647	2.879	1.511	0.662		MM
27	0.049	0.296	1.316	0.048	0.000	0.513	2.282	1.735	0.577	Sample Length (25-36)	36.848
28	0.045	0.355	1.579	0.058	-0.013	0.612	2.722	1.724	0.580		
29	0.048	0.312	1.388	0.051	-0.003	0.552	2.456	1.770	0.565		
30	0.043	0.282	1.252	0.046	-0.003	0.526	2.342	1.870	0.535		
31	0.059	0.401	1.783	0.066	-0.007	0.671	2.983	1.673	0.598		
32	0.033	0.240	1.067	0.039	-0.006	0.459	2.042	1.913	0.523		
33	0.054	0.345	1.533	0.056	-0.003	0.614	2.730	1.781	0.562		
34	0.065	0.405	1.803	0.066	-0.002	0.686	3.050	1.691	0.591		
35	0.047	0.349	1.551	0.057	-0.010	0.625	2.780	1.792	0.558		
36	0.047	0.354	1.576	0.058	-0.011	0.627	2.790	1.770	0.565		
Avg.	0.063	0.390	1.736	0.065	-0.003	0.698	3.107	1.799	0.562		

	Depth of Cut: 0.0102 mm			Initial Cut Velocity: 575 mm/s							
Run	Energy Change [J]	Cutting Force [Lbs]	Cutting Force [N]	Energy of Cutting Force [J]	Work of Thrust [J]	Thrust Force [lb]	Thrust Force [N]	Ratio Thrust/Cutting	Ratio Cutting/Thrust		MM
1	0.165	1.025	4.561	0.173	-0.008	1.113	4.951	1.086	0.921	Sample Length (1-12)	37.944
2	0.209	1.289	5.733	0.218	-0.008	1.225	5.451	0.951	1.052		
3	0.152	0.887	3.945	0.150	0.003	1.021	4.542	1.151	0.869		
4	0.152	0.935	4.159	0.158	-0.005	1.105	4.914	1.182	0.846		
5	0.158	0.959	4.268	0.162	-0.004	1.167	5.190	1.216	0.822		
6	0.194	1.189	5.288	0.201	-0.007	1.237	5.500	1.040	0.961		
7	0.150	0.923	4.107	0.156	-0.006	1.064	4.733	1.152	0.868		
8	0.150	0.922	4.102	0.156	-0.006	1.110	4.938	1.204	0.831		
9	0.144	0.890	3.958	0.150	-0.006	1.087	4.836	1.222	0.818		
10	0.186	1.183	5.264	0.200	-0.014	1.259	5.601	1.064	0.940		
11	0.148	0.886	3.943	0.150	-0.002	1.060	4.717	1.196	0.836		
12	0.182	0.996	4.428	0.168	0.014	1.222	5.437	1.228	0.815		
13	0.111	0.721	3.207	0.121	-0.009	1.076	4.786	1.492	0.670		MM
14	0.130	0.814	3.619	0.136	-0.006	1.203	5.351	1.479	0.676	Sample Length (13-24)	37.613
15	0.132	0.869	3.864	0.145	-0.013	1.282	5.703	1.476	0.677		
16	0.152	0.954	4.242	0.160	-0.007	1.368	6.086	1.435	0.697		
17	0.156	1.032	4.590	0.173	-0.017	1.421	6.320	1.377	0.726		
18		0.981	4.362	0.164		1.368	6.084	1.395	0.717		
19	0.156	0.988	4.395	0.165	-0.009	1.396	6.211	1.413	0.708		
20	0.165	1.039	4.621	0.174	-0.008	1.436	6.390	1.383	0.723		
21	0.156	1.020	4.535	0.171	-0.014	1.411	6.277	1.384	0.723		
22	0.155	0.982	4.370	0.164	-0.010	1.399	6.222	1.424	0.702		
23	0.166	1.067	4.747	0.179	-0.012	1.465	6.517	1.373	0.728		
24	0.174	1.105	4.915	0.185	-0.011	1.482	6.594	1.342	0.745		
25	0.120	0.783	3.485	0.128	-0.009	0.900	4.004	1.149	0.870		
26	0.128	0.835	3.715	0.137	-0.009	0.980	4.357	1.173	0.853		MM
27	0.133	0.887	3.944	0.145	-0.012	1.042	4.635	1.175	0.851	Sample Length (25-36)	36.848
28	0.151	0.990	4.403	0.162	-0.011	1.116	4.966	1.128	0.887		
29	0.142	0.894	3.977	0.147	-0.004	1.047	4.658	1.171	0.854		
30	0.180	1.172	5.215	0.192	-0.012	1.198	5.330	1.022	0.978		
31	0.141	0.911	4.051	0.149	-0.008	1.060	4.715	1.164	0.859		
32	0.148	0.980	4.358	0.161	-0.013	1.131	5.029	1.154	0.867		
33	0.138	0.887	3.947	0.145	-0.007	1.049	4.667	1.183	0.846		
34	0.149	0.954	4.245	0.156	-0.008	1.106	4.919	1.159	0.863		
35	0.149	0.955	4.248	0.157	-0.008	1.113	4.950	1.165	0.858		
36	0.143	0.945	4.204	0.155	-0.011	1.090	4.851	1.154	0.867		
Avg.	0.153	0.968	4.306	0.161	-0.008	1.189	5.290	1.235	0.820		

	Depth of Cut: 0.0025 mm			Initial Cut Velocity: 575 mm/s							
Run	Energy Change [J]	Cutting Force [Lbs]	Cutting Force [N]	Energy of Cutting Force [J]	Work of Thrust [J]	Thrust Force [lb]	Thrust Force [N]	Ratio Thrust/Cutting	Ratio Cutting/Thrust		MM
1	0.088	0.559	2.485	0.094	-0.006	0.714	3.175	1.278	0.783	Sample Length (1-12)	37.944
2	0.076	0.450	2.001	0.076	0.001	0.657	2.921	1.460	0.685		
3	0.088	0.515	2.290	0.087	0.001	0.642	2.857	1.247	0.802		
4	0.055	0.328	1.457	0.055	0.000	0.509	2.262	1.553	0.644		
5	0.072	0.440	1.959	0.074	-0.002	0.637	2.833	1.446	0.691		
6	0.055	0.319	1.418	0.054	0.001	0.523	2.325	1.639	0.610		
7	0.049	0.281	1.249	0.047	0.002	0.466	2.073	1.660	0.602		
8	0.055	0.328	1.459	0.055	0.000	0.555	2.469	1.692	0.591		
9	0.058	0.330	1.466	0.056	0.003	0.473	2.105	1.435	0.697		
10	0.058	0.339	1.508	0.057	0.001	0.555	2.467	1.636	0.611		
11	0.049	0.283	1.258	0.048	0.001	0.489	2.175	1.728	0.579		
12	0.064	0.393	1.747	0.066	-0.002	0.605	2.693	1.541	0.649		
13	0.089	0.558	2.484	0.093	-0.005	0.890	3.958	1.594	0.627		MM
14	0.080	0.491	2.185	0.082	-0.003	0.854	3.799	1.739	0.575	Sample Length (13-24)	37.613
15	0.079	0.482	2.145	0.081	-0.002	0.851	3.786	1.765	0.567		
16	0.075	0.489	2.176	0.082	-0.006	0.851	3.785	1.739	0.575		
17	0.079	0.491	2.186	0.082	-0.003	0.834	3.708	1.696	0.589		
18	0.081	0.540	2.404	0.090	-0.009	0.866	3.851	1.602	0.624		
19	0.051	0.330	1.466	0.055	-0.004	0.628	2.792	1.905	0.525		
20	0.049	0.325	1.444	0.054	-0.006	0.594	2.643	1.831	0.546		
21	0.053	0.338	1.505	0.057	-0.004	0.635	2.824	1.876	0.533		
22	0.055	0.328	1.461	0.055	0.000	0.652	2.900	1.985	0.504		
23	0.073	0.482	2.143	0.081	-0.008	0.817	3.636	1.696	0.590		
24	0.057	0.348	1.549	0.058	-0.001	0.663	2.951	1.906	0.525		
25	0.049	0.372	1.657	0.061	-0.012	0.519	2.309	1.394	0.717		
26	Omitted	0.362	1.609	0.059	N/A	0.532	2.366	1.471	0.680		MM
27	0.046	0.325	1.444	0.053	-0.008	0.498	2.215	1.534	0.652	Sample Length (25-36)	36.848
28	0.045	0.300	1.333	0.049	-0.004	0.459	2.043	1.533	0.652		
29	0.054	0.360	1.603	0.059	-0.005	0.535	2.379	1.484	0.674		
30	0.042	0.322	1.433	0.053	-0.011	0.504	2.243	1.565	0.639		
31	0.042	0.299	1.330	0.049	-0.007	0.479	2.129	1.601	0.625		
32	0.045	0.298	1.327	0.049	-0.004	0.477	2.121	1.599	0.626		
33	0.048	0.336	1.496	0.055	-0.007	0.514	2.285	1.528	0.655		
34	0.050	0.327	1.455	0.054	-0.003	0.506	2.250	1.547	0.647		
35	0.054	0.363	1.614	0.059	-0.006	0.536	2.385	1.477	0.677		
36	0.047	0.307	1.364	0.050	-0.003	0.494	2.197	1.611	0.621		
Avg.	0.060	0.382	1.697	0.064	-0.003	0.611	2.720	1.611	0.627		